Electronic correlations and crystal-field effects in RCu$_3$Ru$_4$O$_{12}$ (R = La, Pr, Nd)

A. Günther,[1] S. Riegg,[2] W. Kraetschmer,[1] S. Wehrmeister,[1] N. Büttgen,[1] E.-W. Scheidt,[3] H.-A. Krug von Nidda,[1,*] M. V. Eremin,[4] E. A. Arkhipova,[4] R. M. Eremina,[5] A. Krimmel,[1,†] H. Mutka,[6] and A. Loidl[1]

[1]*Experimental Physics V, Center for Electronic Correlations and Magnetism, Institute of Physics, University of Augsburg, 86135 Augsburg, Germany*

[2]*Functional Materials, Technical University Darmstadt, 64287 Darmstadt, Germany*

[3]*Chemical Physics and Materials Science, Institute of Physics, University of Augsburg, 86159 Augsburg, Germany*

[4]*Kazan Federal University, 420008 Kazan, Russia*

[5]*Zavoisky Physical-Technical Institute, Federal Research Center "Kazan Scientific Center of RAS," 420029 Kazan, Russia*

[6]*Institut Laue Langevin, BP 156, 38042 Grenoble Cedex 9, France*

(Received 5 September 2019; accepted 28 October 2020; published 16 December 2020)

Among the large class of A-site ordered perovskites of stoichiometry $AC_3B_4O_{12}$, the rare-earth (R) ruthenates RCu$_3$Ru$_4$O$_{12}$ (R = La, Pr, Nd) are interesting compounds due both to Ru-4d-derived electronic correlations and to unconventional crystal-electric-field effects of the R ions. Here we report on detailed investigations of these compounds utilizing x-ray diffraction, neutron scattering, magnetic susceptibility, and electrical resistivity measurements as well as heat capacity and nuclear resonance experiments. A broad range of external parameters is scanned and depending on the specific technique, temperatures range from 100 mK to 730 K in external magnetic fields up to 14 T. In this work LaCu$_3$Ru$_4$O$_{12}$ serves as reference compound with a nonmagnetic A site, characterized in detail recently [S. Riegg *et al.*, Phys. Rev. B **93**, 115149 (2016)]. All compounds investigated reveal heavy-fermion behavior with a T^2 dependence of the low-temperature electrical resistivity and significantly enhanced Sommerfeld coefficients. Toward low temperatures, the compounds with R = Pr and Nd are dominated by the magnetic moments of the R ions, which occupy crystallographic positions with point-group symmetry T_h. The crystal-electric-field effects are clearly visible especially in heat capacity and inelastic neutron scattering data from which the crystal-electric-field parameters are derived. The ground state of the Pr^{3+} ion is identified as a triplet ($\Gamma_4^{(1)}$), whereas for Nd^{3+} it is a quartet (Γ_{67}). Evidence for lowering of the T_h symmetry is observed at the Pr site at temperatures below 10 K, suggesting the formation of orbital order. Moreover, the spin-lattice relaxation derived from ^{63}Cu nuclear quadrupole resonance indicates characteristic temperatures close to 7 K and 350 mK, probably related to orbital and magnetic order, respectively.

DOI: 10.1103/PhysRevB.102.235136

I. INTRODUCTION

Transition-metal compounds of the perovskite-related superstructure $AC_3B_4O_{12}$ are derived from the parent perovskite ABO_3 by substituting three-fourths of the A-site cations by Jahn-Teller active ions. As described by the Glazer notation [1] $a^+a^+a^+$, the octahedra are rotated around ⟨111⟩ such that the bond angle B-O-B is lowered to approximately 140° compared to 180° in the ideal perovskite. This tilting imposes a profound modification of the anionic environment of three-fourths of the original A site and leads to the appearance of a new crystallographic C site which implies a doubling of the unit cell in all three directions while leaving the cubic symmetry intact [2]. Thereby, the C-O distances undergo serious changes, eventually resulting in an almost square-planar coordination similar to the CuO_2 planes in the high-T_c cuprates [3,4].

A more general derivation of the 1:3 A-site ordered perovskites is given by a group-theoretic approach which regards the structural formation as a phase transition from the archetype perovskite ($Pm\bar{3}m$) to the respective $AC_3B_4O_{12}$ structure [5]. A set of order parameters is used to describe this transformation.

The $AC_3B_4O_{12}$ compounds drastically change their physical properties when chemically substituted in any position, which gives rise to a large variety of fascinating material characteristics. For example, CaCu$_3$Ti$_4$O$_{12}$ has been extensively studied with respect to colossal dielectric properties [6,7], whereas CaCu$_3$Mn$_4$O$_{12}$ is a ferromagnet with an ordering temperature as high as T_c = 360 K and high magnetoresistance [8,9].

CaCu$_3$Ru$_4$O$_{12}$ was reported to exhibit heavy-fermion (HF) properties [10,11] and was originally interpreted as a direct analog to conventional f-electron HF systems as well with localized magnetic moments of Cu^{2+} ions and itinerant Ru-derived d electrons exhibiting strong Ru-O hybridization [10]. Localized and itinerant electrons were supposed to be coupled antiferromagnetically by the Kondo mechanism [12]. However, the formation of the HF state by the Kondo effect

*hans-albrecht.krug@physik.uni-augsburg.de

†Present address: Academy for Refrigeration and AC (ESaK), Theo-Mack-Strasse 3, 63477 Maintal, Germany.

at the Cu site has been questioned in favor of correlations within the Ru band states by a systematic investigation of the series $ACu_3Ru_4O_{12}$ (A = Na, $Na_{0.5}Ca_{0.5}$, Ca, $Ca_{0.5}La_{0.5}$, La) [13] and detailed NMR measurements of $CaCu_3Ru_4O_{12}$ [14]. Additionally, $CaCu_3Ru_4O_{12}$ shows non-Fermi-liquid (NFL) properties below 2 K [11] and has been characterized as the first example of an intermediate-valence system among transition-metal compounds [15]. A further key result was obtained by site-sensitive NMR experiments probing strongly enhanced effective masses at the Ru site concomitantly with reduced masses at the Cu site. This strongly supports the hypothesis that the HF formation takes place at the Ru site. Ti substitution in $LaCu_3Ru_4O_{12}$ corroborated the Kondo effect at the Ru^{4+} spins to be the driving force of the electronic mass enhancement similar to conventional $4f$-electron-based heavy-fermion compounds [16].

In this work we focus on the metallic ruthenates $RCu_3Ru_4O_{12}$ (R = La, Pr, Nd), which were originally characterized as Pauli paramagnets displaying valence degeneracy [17]. Moreover, they show enhanced Sommerfeld coefficients indicative of strong electronic correlations [10,13]. From the lanthanides only La, Pr, and Nd [18–20] can be substituted at the A site of $ACu_3Ru_4O_{12}$ since smaller ions seem to destabilize the structure.[1] Structural studies on $RCu_3Ru_4O_{12}$ (R = La, Pr, Nd) as well as data on transport properties, magnetic susceptibility, spectroscopy, and magnetic resonance have been published previously [3,13,16–36]. Here we report detailed low-temperature properties including structural details, local and bulk magnetism, electrical resistivity, and specific heat. We find typical correlated electron behavior, however with a specific and interesting interference of correlated band states with low-lying crystal-electric-field (CEF) levels. The CEF will be of fundamental importance for the magnetic low-temperature properties of the investigated compounds. In addition, in HF compounds the size of the CEF splitting has to be compared with the characteristic temperature of the electronic correlation effect. As detailed in the seminal work by Lea *et al.* [37] more than 50 years ago, praseodymium and neodymium compounds can behave drastically different, even in cubic symmetry: Pr^{3+} with total angular momentum $J = 4$, in a cubic CEF splits into a nonmagnetic singlet, a nonmagnetic doublet, and two magnetic triplets, providing the realistic possibility to find compounds with zero magnetic moment at low temperatures and hence a nonmagnetic ground state; Nd^{3+} with $J = 9/2$ in cubic symmetry splits into one magnetic doublet and two magnetic quartets and hence always will exhibit a finite magnetic moment even at the lowest temperatures.

The properties of $PrCu_3Ru_4O_{12}$ turned out to be naturally in line with recent investigations on compounds with rare-earth ions in T_h point-group symmetry. The R ion in this compound is surrounded by 12 oxygen ions, similar to the filled skutterudite compound $PrTa_2Al_{20}$ in which the R ion is surrounded by 12 Al ions [38]. Here the CEF leads to a nonmagnetic Γ_3 doublet ground state of the Pr ion. Therefore, $PrTa_2Al_{20}$ is a good playground to investigate antiferroquadrupolar (AFQ) ordering. Exotic quadrupolar phenomena in non-Kramers doublet systems are also observed in the cases of PrT_2Zn_{20} (T = Ir, Rh) and PrT_2Al_{20} (T = V, Ti) [39]. In particular, the $PrRh_2Zn_{20}$ becomes superconducting below $T = 0.06$ K [40]. Furthermore, the discovery of heavy-fermion superconductivity [41] and adjacent AFQ order [42] in $PrOs_4Sb_{12}$ suggested a new type of superconducting (SC) pairing mechanism. The observed SC transition temperature $T_c = 1.85$ K in $PrOs_4Sb_{12}$ is considerably higher than that of $LaOs_4Sb_{12}$ ($T_c = 0.74$ K). This fact indicates that the superconductivity involves $4f$ electrons of Pr [43]. In this case the ground state of the Pr ion is a singlet (Γ_1). Another fascinating compound is PrPd3S4. Recently, it attracted much attention as a possible candidate for the formation of unconventional fermionic quasiparticles [44]. Here the site symmetry is also T_h and it is expected that the Pr ground state is degenerate and therefore may undergo quadrupolar ordering [45].

After presenting the experimental results obtained in $RCu_3Ru_4O_{12}$ (R = La, Pr, Nd), we will provide the theoretical background for the crystal-field analysis of the R ions at the A site and discuss the cases of Pr^{3+} and Nd^{3+}. We will especially concentrate on $PrCu_3Ru_4O_{12}$, where we will argue that at low temperatures the degeneracy of the ground-state triplet Γ_4 of the Pr^{3+} ion is further lifted by a crystal lattice distortion or a cooperative orbital order effect. This conclusion is based on heat capacity, magnetic susceptibility, Cu nuclear quadrupole resonance (NQR) relaxation, neutron scattering data, and the calculated CEF energy-level scheme for the Pr^{3+} ($^3H_4$) state.

II. EXPERIMENTAL DETAILS AND RESULTS

Polycrystalline samples of $RCu_3Ru_4O_{12}$ (R = La, Pr, Nd) were synthesized by solid-state reactions [18] and characterized by x-ray powder diffraction (XRD) with Cu $K_{\alpha 1}$ radiation, using a position sensitive detector (STOE Stadi P). Additional structural investigations were performed by neutron powder diffraction (NPD) on the high-resolution powder diffractometer for thermal neutrons [46] at the Paul Scherrer Institut, Switzerland ($\lambda = 1.1545$ Å). The samples were filled in cylindrical vanadium cans and mounted in a cryostat capable of $1.6\ \mathrm{K} \leqslant T \leqslant 300$ K. Both XRD and NPD data were analyzed by Rietveld refinement [47] using the FULLPROF program suite [48]. Magnetic measurements were performed with a superconducting quantum interference device (SQUID) magnetometer (Quantum Design MPMS5 XL) in applied fields up to 5 T and in the temperature range $1.8\ \mathrm{K} \leqslant T \leqslant 400$ K, extended with the oven option up to 730 K.

Four-point electrical resistivity was measured on pressed and sintered ceramics for $2\ \mathrm{K} \leqslant T \leqslant 300$ K in zero field and in magnetic fields up to 14 T in different cryomagnets (Oxford Instruments Teslatron/Quantum Design PPMS). Both a DC (current source and nanovoltmeter: Keithley 2400 and 182) and an AC technique (resistance bridge: Quantum Design Model 7100, $f = 1$ Hz) were applied. In addition, measurements down to 100 mK have been performed in a $^3He/^4He$ dilution cryostat using an AC resistance bridge (Linear Research LR700).

[1]Note that the ionic radius of Nd^{3+} (127 pm, coordination 12) seems to be the smallest possible one. Sample preparation with Sm^{3+} and all heavier (i.e., smaller) R ions is not successful under ambient pressure. Furthermore, Ce^{3+} seems to be oxidized to Ce^{4+} (114 pm, coordination 12) during preparation.

The heat capacity was investigated in a physical properties measurement system (Quantum Design PPMS) in the temperature range 1.8 K $\leqslant T \leqslant$ 300 K in zero field and in external fields up to 9 T. The specific-heat measurements were extended down to 100 mK in a ^{3}He/^{4}He dilution cryostat using a relaxation method [49].

Nuclear quadrupole resonance measurements were performed using a phase-coherent pulse spectrometer and spin-echo techniques. The irradiation frequencies for the $\pm 1/2 \leftrightarrow \pm 3/2$ transition of the ^{63}Cu isotope were in the range of 18.8 MHz $< \nu_Q <$ 18.92 MHz for 0.1 K $< T <$ 20 K. Low temperatures were achieved in a top-loading ^{3}He/^{4}He dilution cryostat (Oxford Instruments Kelvinox TLM) with the sample inside the mixing chamber. The spin-lattice relaxation rates $1/T_1$ were obtained by inversion-recovery pulse sequences, where $\tau = 3$ μs was the length of the inverting pulse.

Inelastic neutron-scattering experiments were carried out in the temperature range 1.6 K $\leqslant T \leqslant$ 200 K on the time-of-flight (TOF) spectrometer IN4 at the Institut Laue Langevin, France. An incident neutron wavelength of 2.181 Å was utilized corresponding to an energy of 17.19 meV. An empty can and a vanadium standard have been additionally measured to account for background and detector efficiency, respectively. The raw data were corrected in a standard way employing the LAMP program package [50] converting TOF to energy transfer and a constant wave vector (Q) or energy-transfer (ω) mapping finally resulting in the dynamic structure factor $S(Q, \omega)$. The large-angle detector bank of the spectrometer covers a range of wave-vector transfers of 0.75 Å$^{-1} \leqslant Q \leqslant$ 5.2 Å^{-1} in the elastic channel for the selected wavelength.

A. X-ray and neutron powder diffraction

The crystal structure of RCu$_3$Ru$_4$O$_{12}$ (R = La, Pr, Nd) (see Fig. 1) can be considered as a 2 × 2 × 2 superstructure of the parent perovskite ABO$_3$. It is described by the cubic space group $Im\bar{3}$ (No. 204) and atomic positions of R = La, Pr, Nd at (0,0,0), Cu at ($\frac{1}{2}$, 0, 0), Ru at ($\frac{1}{4}$, $\frac{1}{4}$, $\frac{1}{4}$), and O at (x, y, 0).

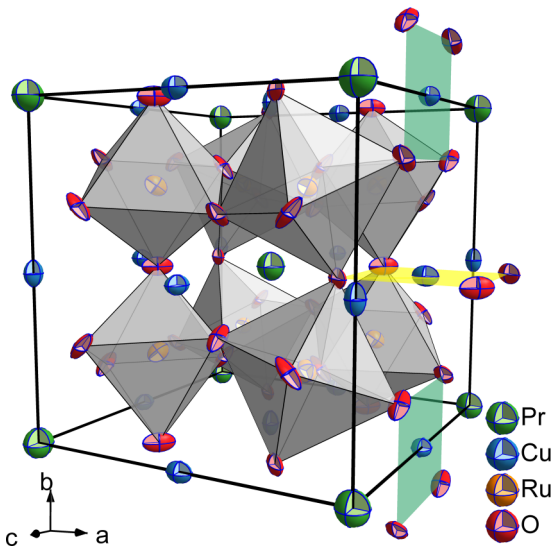

FIG. 1. Unit cell of PrCu$_3$Ru$_4$O$_{12}$ at room temperature derived from NPD including plots of the thermal ellipsoids (99.9% probability level). The octahedra depict the tilted RuO$_6$ units. On the right cell face, the CuO$_4$ plaquettes are indicated by yellow/green planes. In the other investigated compounds the Pr site is occupied by La or Nd.

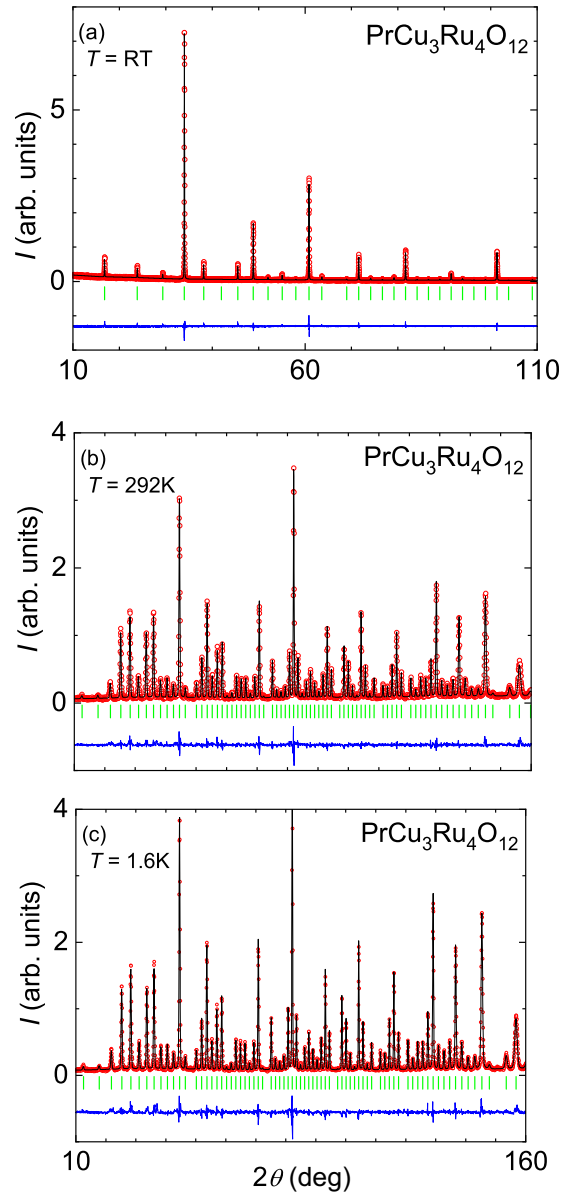

FIG. 2. Powder-diffraction patterns of PrCu$_3$Ru$_4$O$_{12}$ derived from (a) x-ray- and (b) and (c) neutron-scattering experiments at various temperatures. Measured (open red circles) and calculated (black line) intensities, as well as their difference (blue line at the bottom, shifted to negative values for clear depiction) and corresponding Bragg-peak positions (green vertical bars) are shown.

X-ray powder diffraction at room temperature (RT) reveals single-phase material without any indications of impurities. Figure 2(a) shows the corresponding diffraction pattern of PrCu$_3$Ru$_4$O$_{12}$ which is also representative for the La and Nd compound with respect to purity. Excellent agreement between observed and calculated intensities is achieved as indicated by low χ^2 and Bragg reliability factors summarized in Table I along with the cell parameters for all compounds under investigation.

TABLE I. Lattice constant a, oxygen positional parameters x and y, and reliability factors R_{Bragg}, R_{p}, R_{wp}, R_{exp}, and χ^2 of $R\mathrm{Cu_3Ru_4O_{12}}$ (R = La, Pr, Nd) resulting from the XRD and NPD Rietveld refinements at given temperature T.

A	Method	T (K)	a (Å)	x	y	R_{Bragg} (%)	R_{p} (%)	R_{wp} (%)	R_{exp} (%)	χ^2
La	XRD	RT	7.48340(4)	0.17177(110)	0.30228(91)	9.37	7.72	10.8	7.84	1.89
La	NPD	175	7.47545(1)	0.17381(13)	0.30675(13)	4.23	6.24	7.90	4.47	3.12
Pr	XRD	RT	7.45203(6)	0.17264(114)	0.30310(88)	4.63	10.5	14.3	11.2	1.63
Pr	NPD	175	7.45736(1)	0.17329(17)	0.30557(16)	7.67	9.95	11.9	7.10	1.96
Pr	NPD	292(1)	7.46275(1)	0.17369(17)	0.30586(16)	3.67	7.02	9.22	7.09	1.69
Nd	XRD	RT	7.46001(6)	0.17829(169)	0.30821(177)	4.74	9.43	12.8	13.25	0.93
Nd	NPD	175	7.45557(1)	0.17236(16)	0.30548(15)	5.38	6.12	7.86	4.28	3.38

Neutron powder diffraction measurements reveal neither structural phase transitions nor magnetic Bragg peaks, the latter implying the absence of long-range magnetic order down to $T = 1.6$ K, as exemplarily documented by the comparison of the NPD patterns for $\mathrm{PrCu_3Ru_4O_{12}}$ taken at RT and 1.6 K in Figs. 2(b) and 2(c). The diffraction patterns were analyzed by Rietveld refinement; the corresponding calculated values are listed in Table I. That the rare-earth compounds investigated do not order down to at least 1.5 K also becomes evident from the magnetic susceptibility measurements, which will be discussed in the next section.

The structural parameters derived from the neutron data correspond well with data reported in the literature [18–20]. As indicated by the refined anisotropic displacement factors listed in Table II and plotted in Fig. 1 for $\mathrm{PrCu_3Ru_4O_{12}}$, the oxygen atoms feature a preferred vibrational direction within the faces of the unit cell demonstrating the rotation of the $\mathrm{RuO_6}$ octahedra around ⟨111⟩. Ru and Cu have small anisotropic displacements only, Ru along the cell diagonal ⟨111⟩ and Cu along the main cell axes ⟨100⟩, while Pr is confined to an isotropic displacement due to local symmetry restrictions [52,53].

The temperature-dependent lattice parameters and oxygen positions of $R\mathrm{Cu_3Ru_4O_{12}}$ (R = La, Pr, Nd) are shown in Fig. 3. The experimental data can be described utilizing the phenomenological model

$$a(T) = a_0[1 + \alpha\Theta/(e^{\Theta/T} - 1)],$$

where a_0 is the lattice constant at 0 K, α the high-temperature thermal expansion coefficient, and Θ the characteristic Einstein temperature [54]. We would like to point out that in all $R\mathrm{Cu_3Ru_4O_{12}}$ systems investigated in the course of this work, the direct crystallographic environment of the Ru ions is quite similar and not significantly influenced by the different rare-earth ions. This stems from the fact that the ruthenium ions are embedded within oxygen octahedra and the outer electronic configuration of the rare earth ions is rather similar. As documented in Fig. 3, the lattice constants and thermal expansion are very similar for all three compounds. In addition, the Ru-O distances are the same for La, Pr, and Nd (1.99 ± 0.005 Å) and the $\mathrm{RuO_6}$ octahedra are not distorted, as documented by the site symmetry in the relevant space group.

A good description of the thermal expansion is achieved with the resulting parameters listed in Table III. This detailed investigation of the temperature dependence of the lattice parameter has been motivated by findings in $\mathrm{CaCu_3Ru_4O_{12}}$, which have been interpreted in terms of a volume anomaly driven by a valence instability [15]. No similar effects can be detected for $R\mathrm{Cu_3Ru_4O_{12}}$ (R = La, Pr, Nd). The insets of Fig. 3 demonstrate that the oxygen position remains almost constant with respect to temperature, manifesting a Ru-O-Ru bond angle of approximately 140°. Note that the derived values of Θ significantly differ from those obtained from specific-heat data. This is due to the fact that temperatures

TABLE II. Anisotropic displacement factors U_{cif}^{ij} of $R\mathrm{Cu_3Ru_4O_{12}}$ (R = La, Pr, Nd) according to the conventions given by Grosse-Kunstleve and Adams [51] They were derived from the refinement of the NPD patterns at temperature T for each constituent atom with corresponding crystallographic site and local symmetry [52,53].

T (K)	Atom	Site	Symmetry	U_{cif}^{11} (Å^2)	U_{cif}^{22} (Å^2)	U_{cif}^{33} (Å^2)	U_{cif}^{12} (Å^2)	U_{cif}^{13} (Å^2)	U_{cif}^{23} (Å^2)
175	A = La	2*a*	*m*$\bar{3}$.	0.0026(4)	U_{11}	U_{11}	0	0	0
175	Cu	6*b*	*mmm*..	0.0029(6)	0.0059(6)	0.0016(6)	0	0	0
175	Ru	8*c*	.$\bar{3}$.	0.00236(16)	U_{11}	U_{11}	−0.0002(3)	U_{12}	U_{12}
175	O	24*g*	*m*..	0.0037(3)	0.0042(4)	0.0045(4)	0.0006(3)	0	0
173(1)	A = Pr	2*a*	*m*$\bar{3}$.	0.0058(10)	U_{11}	U_{11}	0	0	0
173(1)	Cu	6*b*	*mmm*..	0.0020(8)	0.0025(7)	0.0019(8)	0	0	0
173(1)	Ru	8*c*	.$\bar{3}$.	0.00132(18)	U_{11}	U_{11}	0.0001(2)	U_{12}	U_{12}
173(1)	O	24*g*	*m*..	0.0054(5)	0.0047(4)	0.0020(4)	0.0022(4)	0	0
175	A = Nd	2*a*	*m*$\bar{3}$.	0.0014(5)	U_{11}	U_{11}	0	0	0
175	Cu	6*b*	*mmm*..	0.0016(7)	0.0039(7)	0.0004(7)	0	0	0
175	Ru	8*c*	.$\bar{3}$.	0.0013(2)	U_{11}	U_{11}	−0.0002(3)	U_{12}	U_{12}
175	O	24*g*	*m*..	0.0024(4)	0.0028(4)	0.0030(5)	0.0003(4)	0	0

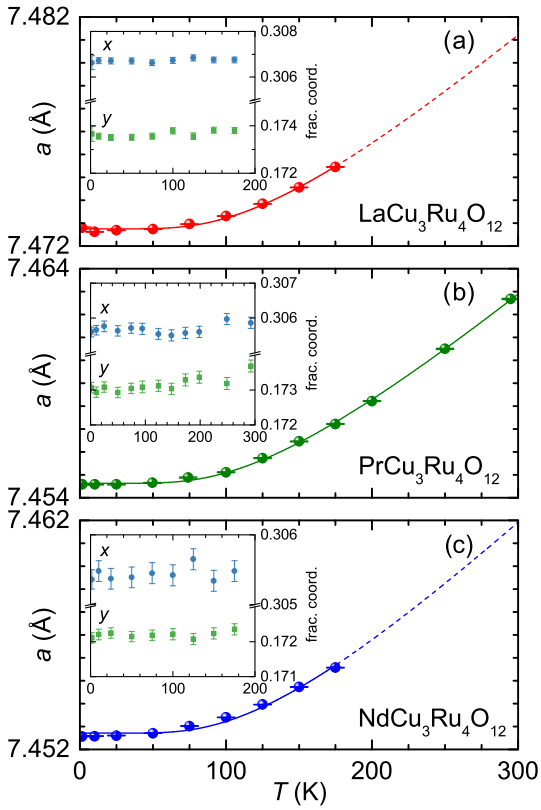

FIG. 3. Temperature-dependent lattice parameter a of (a) $LaCu_3Ru_4O_{12}$, (b) $PrCu_3Ru_4O_{12}$, and (c) $NdCu_3Ru_4O_{12}$, resulting from the Rietveld refinements of the NPD measurements. The solid lines (dashed where no data are available) are fits to the thermal expansion. See the text for details. The insets show the refined positional parameters of oxygen expressed in fractional coordinates (x and y).

are fitting parameters corresponding to effective values and taking into account all acoustic and optical phonons. Details about the evaluation of thermal expansion data can be found in Ref. [54].

B. Magnetic susceptibility

The magnetic susceptibilities and the inverse susceptibilities of all three R compounds, as measured in an external magnetic field of 1 T, are shown in Fig. 4 together with the data of $CaCu_3Ru_4O_{12}$ [11]. A rough first inspection makes clear that the Pr and the Nd compound are characterized by Curie-Weiss (CW) laws, dominated by the rare-earth ions.

TABLE III. Lattice parameters a_0, high-temperature thermal expansion coefficient α, and Einstein temperature Θ of $RCu_3Ru_4O_{12}$ (R = La, Pr, Nd) as resulting from the fit to the temperature-dependent lattice constant. See the text for details.

Compound	a_0 (Å)	α (10^{-6} K^{-1})	Θ (K)
$LaCu_3Ru_4O_{12}$	7.47275(3)	7.74(21)	390
$PrCu_3Ru_4O_{12}$	7.45463(3)	7.56(5)	389(11)
$NdCu_3Ru_4O_{12}$	7.45271(6)	8.46(39)	390

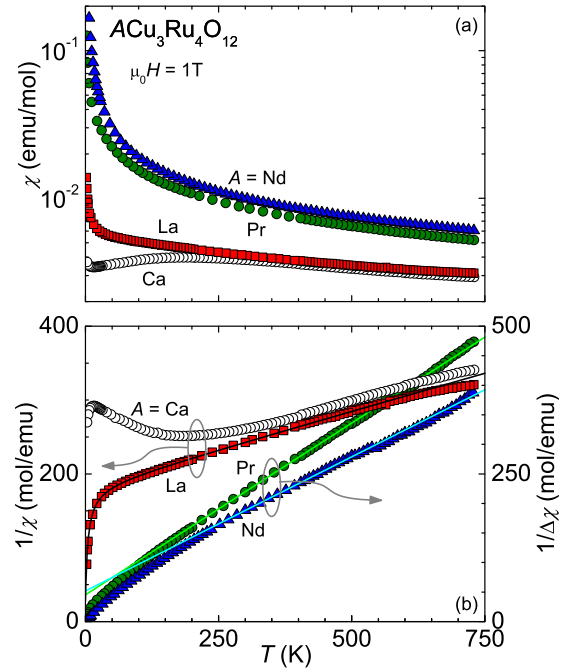

FIG. 4. (a) Temperature-dependent magnetic susceptibility χ of polycrystalline $RCu_3Ru_4O_{12}$ (R = La, Pr, Nd) in a semilogarithmic representation and (b) its inverse in an external field of 1 T. The data of $CaCu_3Ru_4O_{12}$ are included for comparison (up to 400 K from Ref. [11], extended to 730 K). The data of the inverse susceptibility of $RCu_3Ru_4O_{12}$ (R = Pr, Nd) have been calculated by subtraction of the reference compound $LaCu_3Ru_4O_{12}$. The solid lines are fits according to a (single) Curie-Weiss law (R = Pr, Nd) and a double Curie-Weiss law (R = La) [16]. See the text for details.

The La and Ca compound can be viewed as pure correlated metals, but only the Ca compound reveals a broad cusp in the magnetic susceptibility close to 180 K, which earlier was identified as the characteristic temperature $T^\star$, indicative of the onset of spin or charge fluctuations, and roughly can be identified with the Kondo temperature [11]. In canonical Kondo or valence-fluctuation systems it documents the transition from localized electronic states at high temperatures to itinerant band states at low temperatures. In the La compound this specific anomaly indicating a characteristic temperature $T^\star$ is missing. In the Pr and Nd compound these anomalies possibly are screened by the large paramagnetic contributions from the rare-earth ions. In these cases where a characteristic temperature cannot be identified by an anomaly in the magnetic susceptibility, one can estimate the characteristic temperature by the high-temperature CW behavior: One assumes as a rule of thumb [55] that $T^\star \approx |\theta_{CW}|/4$, which in the Ca compound gives the right order of magnitude for the characteristic Kondo-type temperature. Here we speculate that spin fluctuations with a characteristic temperature $T^\star$ also exist in all the rare-earth ruthenium compounds; however, the Ru valence in these compounds seems to be relatively stable down to low temperatures.

Turning now to the Pr and Nd compound, it is clear that these are dominated by the local magnetic moment of the R ion. To arrive at some definite conclusions, the temperature-dependent susceptibility of the La compound

(which describes the influence of the d electrons of Cu and Ru ions) is subtracted from the Pr and Nd data, respectively. The remaining contribution is attributed to the susceptibility of the R ion. In Fig. 4(b) we show the inverse of the difference susceptibility $\Delta\chi = \chi(R\mathrm{Cu_3Ru_4O_{12}}) - \chi(\mathrm{LaCu_3Ru_4O_{12}})$ vs temperature, where R stands for Pr and Nd, respectively. A CW fit for $T > 300$ K reveals paramagnetic moments of $3.71\mu_B/\mathrm{Pr}^{3+}$ and $4.20\mu_B/\mathrm{Nd}^{3+}$ (free-ion values $3.58\mu_B/\mathrm{Pr}^{3+}$ and $3.63\mu_B/\mathrm{Nd}^{3+}$). Note that the resulting CW temperatures have no significance and stem from details of the CEF levels. With decreasing temperature, the data begin to deviate from a linear dependence, which also is attributed to CEF effects of the R ions [56].

For $\mathrm{PrCu_3Ru_4O_{12}}$ the slope of the inverse magnetic susceptibility [see Fig. 4(b)] begins to deviate from the free-ion value roughly below 170 K, which indicates an overall CEF splitting of at least this value. The inverse magnetic susceptibility of the neodymium compound [Fig. 4(b)] begins to deviate at slightly higher temperatures below roughly 220 K. This fact indicates that the population of the CEF levels in $\mathrm{NdCu_3Ru_4O_{12}}$ is evenly distributed above this temperature and that the total splitting is of the same order of magnitude or slightly higher than in the praseodymium system.

Now we focus on the low-temperature behavior of the magnetic susceptibilities, which in the Pr and Nd compound are dominated by the lowest-lying CEF levels. When comparing the increase of the inverse susceptibilities starting from zero temperature, the slopes of the inverse susceptibilities allow an estimate of the effective moments and hence give some hints about the possible ground states of the magnetic ions involved. The Pr compound exhibits a significantly stronger increase giving an estimate of $\mu_{\mathrm{eff}} \approx 1.8\mu_B/\mathrm{Pr}^{3+}$, implying a nontrivial ground state, different from the nonmagnetic singlet often found for non-Kramers ions. To clarify its nature we investigated the magnetic susceptibility applying different magnetic fields as shown later in Fig. 19. The experimental data and corresponding modeling will be discussed in Sec. III B. The slope for the Nd compound is more moderate and gives an effective moment $\mu_{\mathrm{eff}} \approx 2.8\mu_B/\mathrm{Nd}^{3+}$ reduced with respect to the high-temperature value as typical for the ground-state doublet or quartet of Kramers ions.

C. Electrical resistivity

Figure 5 shows the electrical resistivity of polycrystalline $R\mathrm{Cu_3Ru_4O_{12}}$ (R = La, Pr, Nd). Metallic conductivity ($d\rho/dT > 0$) is observed in the entire temperature range with a quadratic temperature dependence $\rho(T) = \rho_0 + AT^2$ for $T < 25$ K, characteristic of a Fermi-liquid (FL) behavior. The absolute values of the La compound correspond well with those reported in the literature [20,21]. The Pr and the Nd compound exhibit higher (residual) resistivities than $\mathrm{LaCu_3Ru_4O_{12}}$, but all three compounds roughly reveal the same residual resistance ratios (RRRs) of approximately 2. Fits of the low-temperature data (not shown) yield residual resistivities and coefficients as listed in Table IV. An estimate of the Kadowaki-Woods ratio reveals values approximately 10–50 times lower than the universal value of 10^{-5} Ω cm mol^2 K^2/J^2 usually found in HF compounds [57].

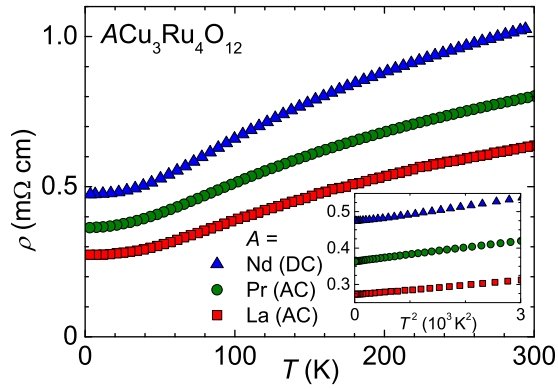

FIG. 5. Temperature-dependent AC and DC resistivity ρ of polycrystalline $R\mathrm{Cu_3Ru_4O_{12}}$ (R = La, Pr, Nd). The inset shows the data in a ρ vs T^2 representation.

The low-temperature resistivity is shown in Fig. 6 for $\mathrm{PrCu_3Ru_4O_{12}}$ [Fig. 6(a)] and $\mathrm{NdCu_3Ru_4O_{12}}$ [Fig. 6(b)] for various magnetic fields. As evident from the inset in Fig. 6(a), deviations from FL behavior in the Pr compound become obvious below 4 K in zero field where a steplike decrease signals the freezing out of magnetic scattering of the conduction electrons by thermal depopulation of the first excited CEF level and populating a ground state bearing a small magnetic moment [58–60]. As a result from the Zeeman splitting of the CEF levels, this step becomes strongly smeared out with increasing field [see Fig. 6(a)].

In the Nd compound a steplike decrease of the resistivity might also be present in zero field, though at temperatures below 2 K for which no data are available; however, a steplike decrease similar to that in the Pr compound evolves upon application of moderate magnetic fields (at around 2 T) and becomes almost fully smeared out for 14 T. Compared to $\mathrm{PrCu_3Ru_4O_{12}}$, the effect in the Nd compound is much stronger and extended to higher temperatures. Moreover, the deviation from FL behavior is different from that in the Pr compound as it is positive for $\mu_0 H < 4$ T and suppressed to negative values

TABLE IV. Residual resistivity ρ_0 and the coefficient A of the quadratic contribution resulting from the FL fit to the resistivity data of $R\mathrm{Cu_3Ru_4O_{12}}$ (R = La, Pr, Nd) according to $\rho(T) = \rho_0 + AT^2$. The Kadowaki-Woods ratio A/γ^2 and the residual resistance ratio (RRR) are also listed.

Compound	ρ_0 (10^{-3} Ω cm)	A (10^{-6} Ω cm/K^2)	A/γ^2 (10^{-5} Ω cm mol^2 K^2/J^2)	RRR $\rho(T = 273\ \mathrm{K})/\rho(T = 4.2\ \mathrm{K})$
$\mathrm{LaCu_3Ru_4O_{12}}$	0.313(1)	0.0184(16)	0.095	2.4
$\mathrm{PrCu_3Ru_4O_{12}}$	0.364(1)	0.0195(1)	0.022	2.2
$\mathrm{NdCu_3Ru_4O_{12}}$	0.474(1)	0.0148(13)	0.039	2.2

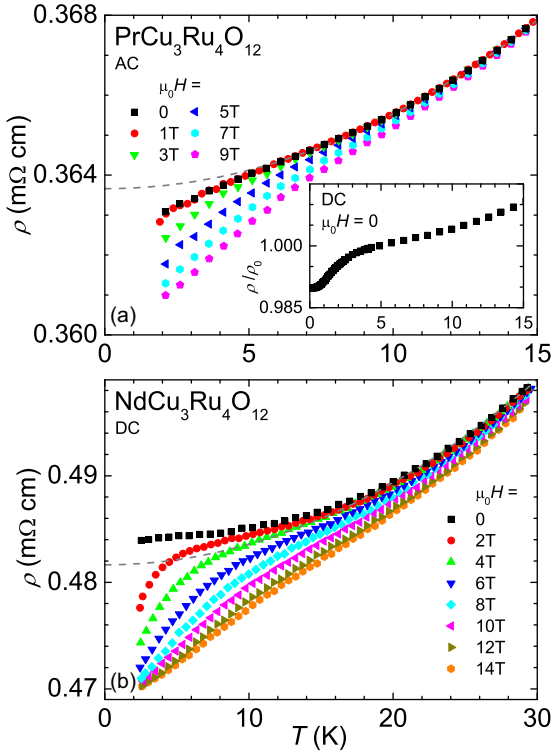

FIG. 6. Temperature-dependent AC and DC resistivity ρ of polycrystalline (a) $PrCu_3Ru_4O_{12}$ and (b) $NdCu_3Ru_4O_{12}$ in various magnetic fields. The inset in (a) shows the normalized DC resistivity ρ/ρ_0 of the Pr compound. The dashed curves are fits to a quadratic temperature dependence and illustrate deviations of the low-temperature experimental data from this behavior.

for higher magnetic fields. Indeed, a magnetic transition at 0.6 K identified in $NdCu_3Ru_4O_{12}$ by NQR recently [61] could be the driving force behind this.

D. Heat capacity

The heat capacity in the representation of C/T vs T of $RCu_3Ru_4O_{12}$ (R = La, Pr, Nd) is shown in Fig. 7 in the temperature range $2\,\mathrm{K} \leqslant T \leqslant 300\,\mathrm{K}$, shifted for clear depiction (see the caption for details). In the inset a C/T vs T^2 representation nicely illustrates the FL behavior according to $C(T) = \gamma T + \beta T^3$. Corresponding fits are indicated by solid lines and the resulting parameters are documented in Table V. $LaCu_3Ru_4O_{12}$ exhibits a quadratic temperature dependence down to lowest accessible temperatures. Its

TABLE V. Sommerfeld coefficient γ, Debye coefficient β, and Debye temperature θ_D resulting from the fit according to conventional Fermi-liquid behavior $C/T = \gamma + \beta T^2$ as shown in the inset of Fig. 7.

Compound	γ (10^{-3} J/mol K^2)	β (10^{-4} J/mol K^4)	θ_D (K)
$LaCu_3Ru_4O_{12}$	135	4.06	169
$PrCu_3Ru_4O_{12}$	295	4.22	166
$NdCu_3Ru_4O_{12}$	178	4.54	162

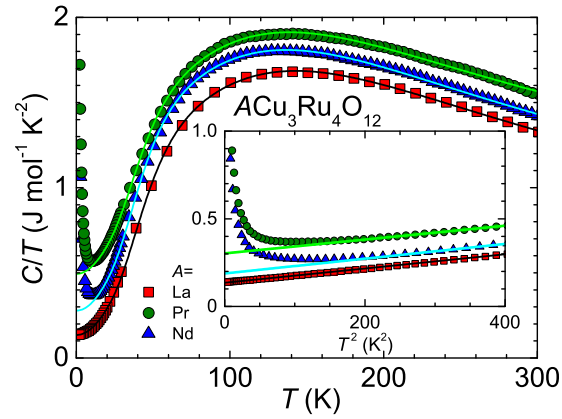

FIG. 7. Temperature-dependent specific heat C in the representation of C/T vs T of polycrystalline $RCu_3Ru_4O_{12}$ (R = La, Pr, Nd) including fits (solid curves) to a Debye-Einstein model of the phononic contribution (data in the main frame have been shifted for clear depiction: Nd, +0.1 and Pr, +0.2 $\mathrm{J mol^{-1} K^{-2}}$). The inset is a representation of C/T vs T^2. The solid lines in the inset are fits according to conventional FL behavior. See Tables V and VI and the text for details.

specific heat also does not depend on external magnetic fields (not shown). For $PrCu_3Ru_4O_{12}$ and $NdCu_3Ru_4O_{12}$ the Fermi-liquid behavior can only be observed down to approximately 15 K due to a strong upturn related to CEF effects, which will be discussed later. All compounds exhibit enhanced Sommerfeld coefficients characteristic for strong electronic correlations. In comparison with the compounds $ACu_3Ru_4O_{12}$ (A = Na, Ca) which have been intensively studied [3,10–15,17–19,21–24,26,27,29,32,62–74], their lanthanide homologues show considerably higher values: 295, 178, and 135 $\mathrm{mJ/mol\,K^2}$ for $RCu_3Ru_4O_{12}$ (R = Pr, Nd, and La), respectively (see also Refs. [13,21,25]). Note that the enhanced Sommerfeld coefficients of the Pr and the Nd compound may partly result from contributions of low-lying CEF levels. Both the Debye temperature derived from the coefficient β via $\theta_D = \sqrt[3]{12R\pi^4/5\beta}$ and the Sommerfeld coefficient γ obtained from the low-temperature data have been fixed for the numerical fit of the specific-heat data up to room temperature. It includes one Debye term

$$C_D = a \times 9R(T/\theta_D)^3 \int_0^{\theta_D/T} x^4 e^x/(e^x - 1)^2 dx$$

and two Einstein terms

$$C_{E1,E2} = (b_1, b_2) \times 3R(\theta_{E1,E2}/T)^2 e^{\theta_{E1,E2}/T}/(e^{\theta_{E1,E2}/T} - 1)^2,$$

TABLE VI. Debye temperature θ_D and Einstein temperatures θ_{E1} and θ_{E2} including weighting factors a, b_1, and b_2 resulting from numerical fits according to a Debye-Einstein model. See Fig. 7 and the text for details.

Compound	$a \times \theta_D$ (K)	$b_1 \times \theta_{E1}$ (K)	$b_2 \times \theta_{E2}$ (K)
$LaCu_3Ru_4O_{12}$	1 × 169	6.5 × 243	10.0 × 594
$PrCu_3Ru_4O_{12}$	1 × 166	5.5 × 234	8.9 × 563
$NdCu_3Ru_4O_{12}$	1 × 162	6.1 × 231	9.5 × 572

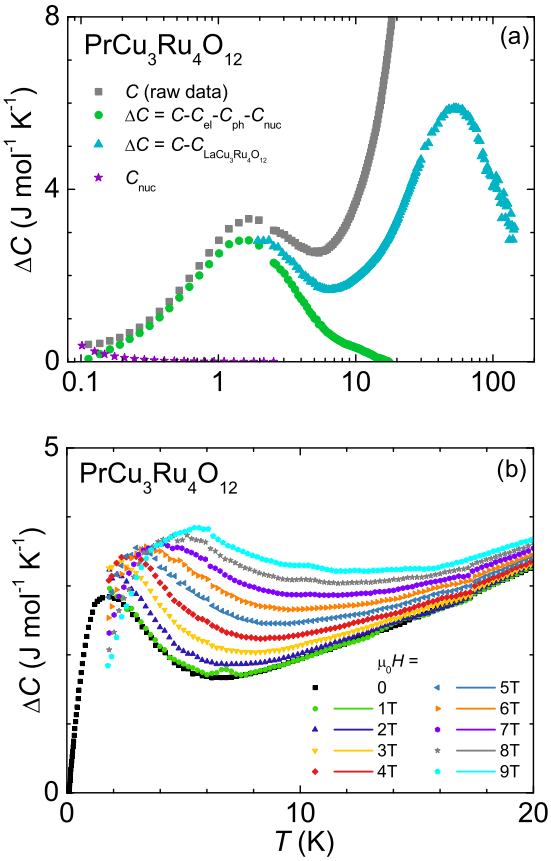

FIG. 8. Temperature-dependent specific heat C of polycrystalline $PrCu_3Ru_4O_{12}$. (a) Experimental zero-field raw data (gray squares) which have been corrected for nuclear (C_{nuc}, purple stars), electronic (C_{el}), and phononic contributions (C_{ph}) resulting in the data set of green circles. Subtraction of the reference compound $LaCu_3Ru_4O_{12}$ results in data represented by blue triangles. (b) Data corrected for the contribution of the reference compound $LaCu_3Ru_4O_{12}$ in various magnetic fields. See the text for details.

with the weighting factors a, b_1, and b_2 and the Einstein temperatures θ_{E1} and θ_{E2}. The weighting a of the Debye term is set to one, corresponding to three degrees of freedom, which account for the contributions of three acoustic phonon modes. The resulting fit parameters are listed in Table VI and describe the experimental data very well (see the solid curves Fig. 7). The sum of the weighting factors theoretically should give the total number of constituents in the formula unit, i.e., 20, but reaches only 17.5, 15.4, and 16.6 for the La, Pr, and Nd compound, respectively. The reason for this might be the existence of further modes at elevated temperatures not included in the fit. The Einstein temperatures exhibit reasonable values at around 235 and 575 K.

A closer look at the specific heat of $PrCu_3Ru_4O_{12}$ is provided in Fig. 8(a). Here the experimental zero-field data (gray squares) clearly show a Schottky-like anomaly at around 2 K, which is obviously related to the transition between low-lying states. The contribution of the CEF becomes even more obvious when subtracting electronic, phononic, and nuclear specific heat. Below 20 K this is done by using the fits according to FL behavior (see Fig. 7 and Table V) as well as by calculating the nuclear contribution to the specific heat (purple stars, only significant well below 0.4 K). The latter includes both literature values [75] of isotope content, nuclear spin I, nuclear magnetic moment μ, quadrupole moment Q and compound-specific parameters, namely, an isotope-specific electric field gradient V_{zz} and a global internal magnetic field $B_{int} = 11.3$ T. The subtraction has been carried out with the parameters β and γ from Table V, $V_{zz}(\mathrm{Cu}-63) = V_{zz}(\mathrm{Cu}-65) = V_{zz}(\mathrm{Pr}-141) = 0.73 \times 10^{22}$ V/m^2, and $V_{zz}(\mathrm{Ru}-99) = V_{zz}(\mathrm{Ru}-101) = 0.43 \times 10^{22}$ V/m^2. The values of V_{zz} are taken from NQR experiments on the homologue compound $CaCu_3Ru_4O_{12}$ and serve here as an upper bound [11]. The resulting data set (green circles) features a pronounced maximum at 1.6 K and vanishes toward 0.1 and 20 K.

To account also for CEF contributions at higher temperatures the specific heat of the reference compound $LaCu_3Ru_4O_{12}$ is subtracted from the experimental data of $PrCu_3Ru_4O_{12}$. Here, another Schottky peak is evident with a maximum at 53 K (blue triangles). When applying magnetic fields, the Schottky anomaly at 2 K continuously shifts to higher temperatures with increasing field, a consequence of the Zeeman splitting of the $4f$ multiplet. This is illustrated in Fig. 8(b), which shows the specific heat corrected for the contribution of the La compound in various magnetic fields.

Turning now to $NdCu_3Ru_4O_{12}$, a similar behavior can be observed. However, the splitting to the first excited level is even smaller than in Pr^{3+}, as can be seen in Fig. 9(a) from the specific heat, although low-temperature data are not on hand and only the onset of a peak in the experimental zero-field data (gray squares) is visible. Due to the fact that this peak emerges from low temperatures upon increasing magnetic fields [see Fig. 9(b)], one can extrapolate its maximum to roughly 1 K. This is in good agreement with recent findings of magnetic order at $T = 0.6$ K [61]. For a more distinct evaluation of the CEF contribution, the electronic and phononic fractions of the specific heat have been subtracted from the experimental zero-field data for $T \leqslant 20$ K with β and γ from Table V. The result is shown by the data set of green circles which represents the high-temperature shoulder of the above-mentioned peak vanishing at around 20 K, similar as in $PrCu_3Ru_4O_{12}$.

Also for the Nd compound, the specific heat of the reference compound $LaCu_3Ru_4O_{12}$ is subtracted from the experimental data in order to account for CEF contributions at higher temperatures. An additional Schottky peak becomes visible with a maximum at 69 K (blue triangles).

On increasing magnetic fields, the anomaly continuously shifts to higher temperatures, even stronger than in the Pr compound but with constant amplitude. This is illustrated in Fig. 9(b), which shows the specific heat corrected for the contribution of the reference compound $LaCu_3Ru_4O_{12}$ in various magnetic fields.

The behavior of the specific-heat maxima with respect to the magnetic field is shown in Fig. 10 for the Pr and the Nd compound. Data are derived from specific heat corrected for the contribution of $LaCu_3Ru_4O_{12}$ [see Figs. 8(b) and 9(b)]. The Pr compound exhibits a quadratic dependence ($T_{max} \propto H^2$) originating from the nonlinear dependence of the ground-state sublevels upon magnetic field typical for non-Kramers

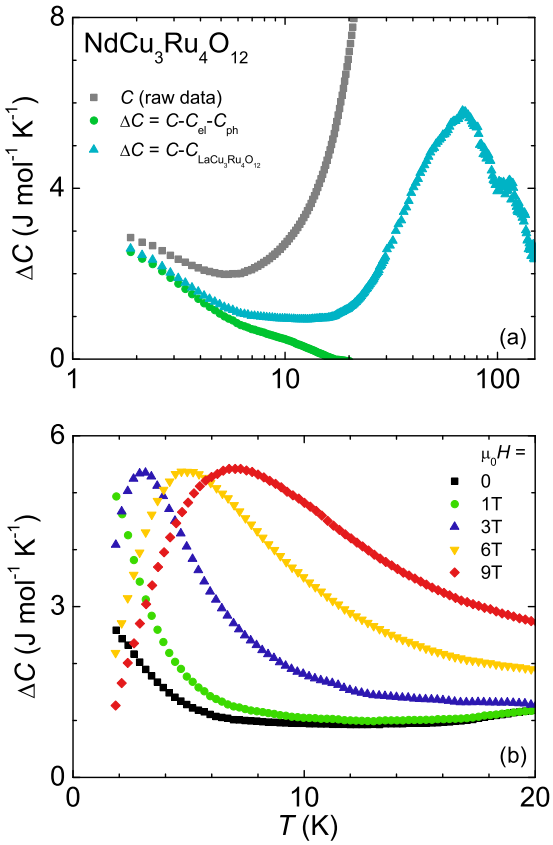

FIG. 9. Temperature-dependent specific heat C of polycrystalline $NdCu_3Ru_4O_{12}$. (a) Experimental zero-field data (gray squares), which have been corrected for electronic (C_{el}) and phononic contributions (C_{ph}) resulting in the data set documented by the green circles. Subtraction of the reference compound $LaCu_3Ru_4O_{12}$ results in data represented by blue triangles. (b) Data (solid symbols) corrected for the contribution of the reference compound $LaCu_3Ru_4O_{12}$ in various magnetic fields. See the text for details.

ions. In contrast, the peak positions of the Nd compound show a linear dependence upon magnetic field as usual for the linear Zeeman effect of Kramers doublets. However, also for the Nd compound, the degeneracy of the ground-state quartet seems to be slightly lifted, as indicated by the nonzero intersection with the temperature abscissa.

E. NMR/NQR

Figure 11 documents Cu NMR spectra of $LaCu_3Ru_4O_{12}$ [Fig. 11(a)] and $PrCu_3Ru_4O_{12}$ [Fig. 11(b)] obtained at 50.25 MHz. For both compounds, the Cu spectra show splittings of the central nuclear transitions $-1/2 \leftrightarrow +1/2$, which are described by the interaction between the nuclear quadrupole moment Q and the electric field gradient at the Cu site up to second-order perturbation theory [11]. Simulated spectra are added at the bottom of each frame in Fig. 11 (light gray area). For $PrCu_3Ru_4O_{12}$, the singularities of the powder spectra are almost smeared out, indicating an increased density of magnetic inhomogeneities compared to $LaCu_3Ru_4O_{12}$. Nevertheless, at $T \approx 2$ K the resonance frequencies ν_{NQR} of the ^{63}Cu transitions for pure quadrupole interaction at zero

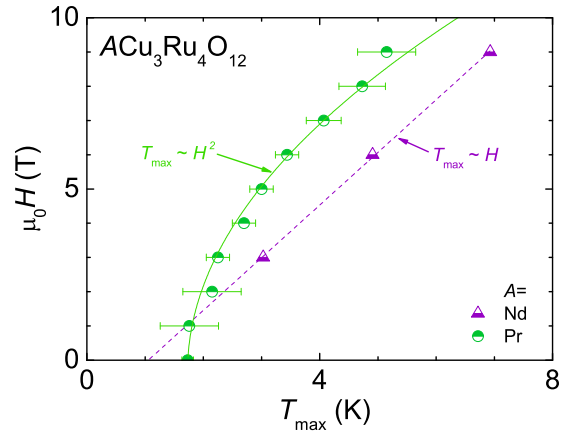

FIG. 10. Field dependence of the experimental peak maxima T_{max} of the lowest CEF transition of $PrCu_3Ru_4O_{12}$ (half filled circles) and $NdCu_3Ru_4O_{12}$ (half filled triangles). The peak maxima are derived from specific-heat data corrected for the contribution of $LaCu_3Ru_4O_{12}$ [see Figs. 8(b) and 9(b)]. The data include estimated error bars for Pr (broad maxima) as well as fits (solid/dashed curve) corresponding to a quadratic/linear dependence of T_{max} with respect to H for Pr/Nd. The regression line for Nd is extrapolated to zero field.

applied magnetic field were found to be $\nu_{NQR} = 19.55$ and 18.83 MHz in $LaCu_3Ru_4O_{12}$ and $PrCu_3Ru_4O_{12}$, respectively. In $LaCu_3Ru_4O_{12}$ an additional Cu signal is observed, also exhibiting a split central transition [highlighted by the dark yellow area at the bottom of Fig. 11(a)]. This splitting directly

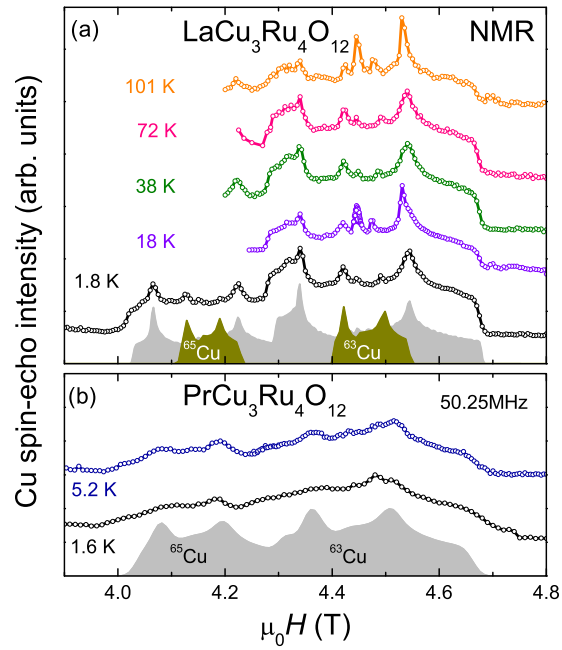

FIG. 11. NMR spectra of the $-1/2 \leftrightarrow +1/2$ transitions of the Cu isotopes ^{63}Cu and ^{65}Cu at $\omega = 50.25$ MHz in (a) $LaCu_3Ru_4O_{12}$ and (b) $PrCu_3Ru_4O_{12}$. The light gray areas at the bottom of each frame indicate the spectra simulation of the quadrupolar perturbed Zeeman splitting. In $LaCu_3Ru_4O_{12}$ an additional Cu signal is observed, also exhibiting a split central transition highlighted by the dark yellow area at the bottom of (a).

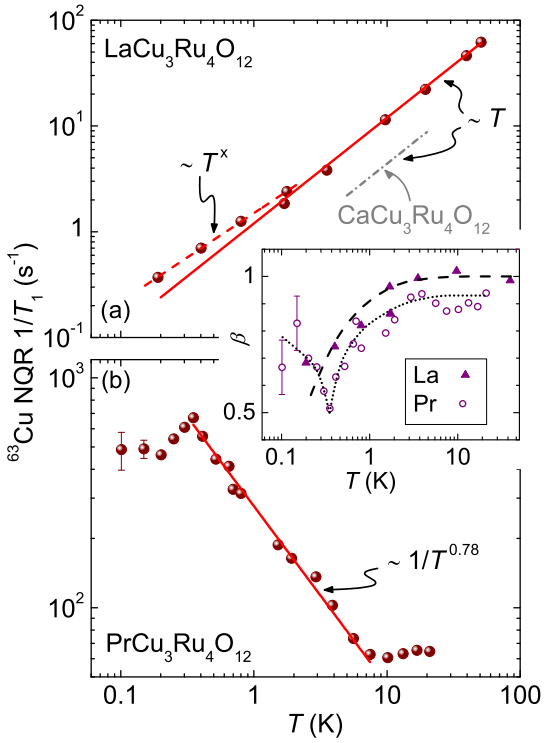

FIG. 12. NQR spin-lattice relaxation rate $1/T_1(T)$ of ^{63}Cu in (a) $LaCu_3Ru_4O_{12}$ and (b) $PrCu_3Ru_4O_{12}$. The solid line in (a) indicates a Korringa law $1/T_1T = 1.2\ \mathrm{s^{-1}\,K^{-1}}$. Additionally, the Korringa law $1/T_1T = 0.44\ \mathrm{s^{-1}\,K^{-1}}$ of $CaCu_3Ru_4O_{12}$ is indicated by the dash-dotted gray line taken from Ref. [11]. The solid line in (b) is a fit to a power law for $0.35\ \mathrm{K} < T < 7.5\ \mathrm{K}$. The inset shows the temperature dependence of the stretching exponent β for $LaCu_3Ru_4O_{12}$ (solid triangles) and $PrCu_3Ru_4O_{12}$ (open circles). The black (dashed/dotted) curves are drawn to guide the eye.

measures the strength of the so-called quadrupole coupling between the nuclear quadrupole moment Q and the surrounding electric field gradient. From the spectrum simulations in Fig. 11(a) it turns out that the quadrupole coupling constant of this additional Cu signal is by a factor of 0.61 smaller than the quadrupole coupling constant of the majority Cu spectral line. This result strongly resembles the case of $YBa_2Cu_3O_{6+\delta}$, where in-chain Cu(1) sites differ by the identical factor of 0.61 from planar Cu(2) sites with respect to their quadrupole coupling constants [76]. Therefore, the additional Cu signal in our NMR spectra indicates the existence of a second species of copper ions with the identical site symmetry, but a different valence state in $LaCu_3Ru_4O_{12}$ corroborating the results of the x-ray absorption near edge structure (XANES) measurements [33].

Figure 12 shows the temperature dependence of the spin-lattice relaxation rate $1/T_1$ of $LaCu_3Ru_4O_{12}$ [Fig. 12(a)] and $PrCu_3Ru_4O_{12}$ [Fig. 12(b)] in a double-logarithmic representation. The values for $1/T_1$ are obtained by irradiating the $\pm 1/2 \leftrightarrow \pm 3/2$ NQR transitions of ^{63}Cu at zero magnetic field as described in Ref. [11]. The spin-lattice relaxation exhibits a temperature-dependent stretching exponent $\beta(T)$, which is given in the inset of Fig. 12. In the case of $LaCu_3Ru_4O_{12}$ a linear behavior $1/T_1 \propto T$ is observed, as indicated by the solid red line in Fig. 12(a). Such linear behavior hallmarks a Korringa law, which is an identifying characteristic of Fermi-liquid properties in $LaCu_3Ru_4O_{12}$. Compared to $CaCu_3Ru_4O_{12}$ [11], where a linear behavior was found for temperatures $5\ \mathrm{K} < T < 20\ \mathrm{K}$ [dash-dotted gray line in Fig. 12(a)], the Korringa constant in $LaCu_3Ru_4O_{12}$ is about three times larger, which implies about $\sqrt{3}$ times larger effective masses m^*. The same enhancement by a factor of around $\sqrt{3}$ is obtained from heat-capacity measurements for the Sommerfeld coefficients γ given above. Deviations from the linear behavior of the Korringa relaxation rate in $LaCu_3Ru_4O_{12}$ appear below 1 K [dashed line in Fig. 12(a)]. Similar effects have been observed in $CaCu_3Ru_4O_{12}$ and have been interpreted as evidence for NFL effects [11]. In $CaCu_3Ru_4O_{12}$ these effects set in below 10 K, while in $LaCu_3Ru_4O_{12}$ NFL behavior certainly is much weaker and significant deviations from Fermi-liquid behavior appear below 1 K only. It is accompanied by clear deviations from pure exponential relaxation ($\beta = 1$). At lowest temperatures significant stretching is indicated by $\beta = 0.7$.

The spin-lattice relaxation in $PrCu_3Ru_4O_{12}$ is considerably faster and exhibits a completely different temperature dependence [Fig. 12(b)]. At elevated temperatures ($7\ \mathrm{K} < T < 20\ \mathrm{K}$) the spin-lattice relaxation rate $1/T_1$ is roughly temperature independent but strongly increases toward lower temperatures ($T < 7$ K). This behavior signals strong spin fluctuations driving the nuclear relaxation. The divergence toward low temperatures tentatively follows a power law $1/T_1 \propto T^{-0.78}$ [red solid line in Fig. 12(b)]. This is close to the critical exponent $\nu = -0.7$, which is given theoretically for the three-dimensional Heisenberg model in the vicinity of a magnetic phase transition [77]. As critical exponents are defined only in a narrow temperature range around T_c, the power law of $1/T_1(T)$ in $PrCu_3Ru_4O_{12}$ rather documents an extended fluctuation regime. At $T \approx 350$ mK, $1/T_1$ shows a maximum. Concomitantly with this anomaly in $1/T_1$, the stretching exponent $\beta(T)$ exhibits a minimum at the same temperature, as indicated in the inset of Fig. 12. The coincidence of a maximum in $1/T_1(T)$ and an accompanying minimum of the stretching exponent $\beta(T)$ at the same temperature resembles the case of $Li_{1-x}Zn_xV_2O_4$ [78], where an identical behavior indicates the transition into a spin-glass state. For $PrCu_3Ru_4O_{12}$, however, a magnetic freezing transition around 350 mK cannot be identified by heat-capacity measurements. Therefore, the maximum of $1/T_1(T)$ rather documents a slowing down of electronic spin fluctuations of timescale τ, which is probed by the nuclear frequency ω of the NQR experiment, where $\omega\tau \approx 1$ with $\omega = 2\pi \times \nu_{\mathrm{NQR}}$.

Comparing the values of the Cu NQR relaxation rates in the La and Pr compound, one concludes that a cross relaxation of the Cu nuclear moment occurs via the Pr ground state. Obviously it should be a doublet or triplet. Its degeneracy is lifted around $T = 10$ K in a small energy interval $\Delta \leqslant k_BT$. The temperature dependence of the relaxation rate will be proportional to the probability difference of up and down transitions [79], i.e.,

$$W_{\mathrm{up}}\left[\exp\left(\frac{\Delta}{k_BT}\right) - 1\right] \approx \mathrm{const}\left(1 + \frac{\Delta}{k_BT} + \cdots\right). \quad (1)$$

The maximum of the relaxation rate at $T = 0.35$ K can be interpreted as a signature of the ordering of magnetic moments

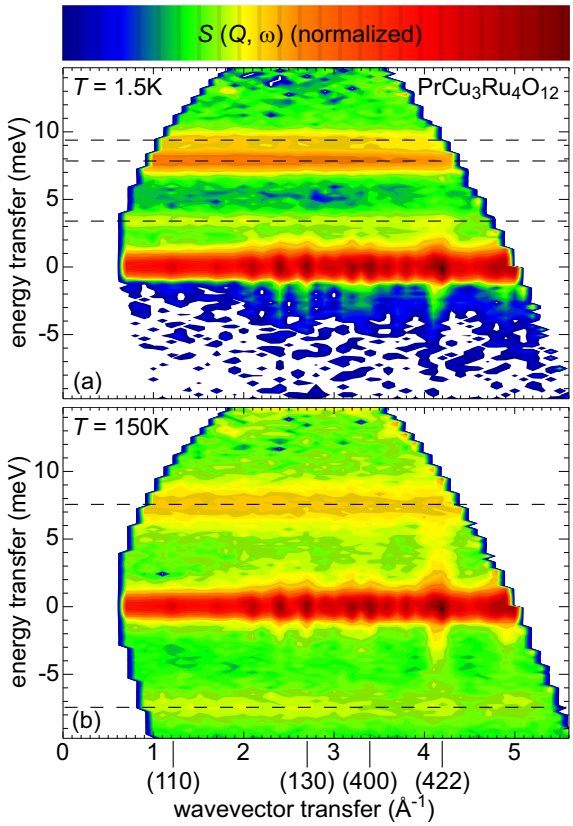

FIG. 13. Contour plot of the dynamic structure factor $S(Q, \omega)$ of $PrCu_3Ru_4O_{12}$ for (a) 1.5 K and (b) 150 K. Intensities are shown by a suitable color coding on a logarithmic scale to indicate increasing intensities from green via yellow and orange to light red above the background level shown in blue. The dashed lines mark the dispersionless intensities as described in the text. Selected nuclear Bragg-peak positions (dark red spots) are indicated by their Miller indices.

of the Pr ions. This assumption is supported by the recent observation of magnetic ordering in $NdCu_3Ru_4O_{12}$ at $T = 0.6$ K [61].

F. Inelastic neutron scattering

To get some more detailed information on the CEF splitting, we performed additional inelastic neutron scattering measurements on $PrCu_3Ru_4O_{12}$. A color-coded contour plot of the dynamic structure factor $S(Q, \omega)$ of $PrCu_3Ru_4O_{12}$ is shown in Fig. 13 for 1.5 K [Fig. 13(a)] and 150 K [Fig. 13(b)]. Both contour plots span momentum transfers of approximately $1\,\text{Å}^{-1} < Q < 5\,\text{Å}^{-1}$ and energy transfers from -10 meV to approximately $+15$ meV. The red riff around zero-energy transfer originates from incoherent scattering with dark red spots corresponding to nuclear Bragg reflections. Additional magnetic scattering is color coded to indicate increasing intensities from green via yellow and orange to light red above the background level shown in blue. At both temperatures dispersionless excitations can be observed in the energy range investigated, which obviously correspond to CEF excitations. At 1.5 K a relatively weak intensity is present at 3.5 meV while well-defined CEF excitations are visible close to 8 and 9.5 meV. At 150 K only the strongest

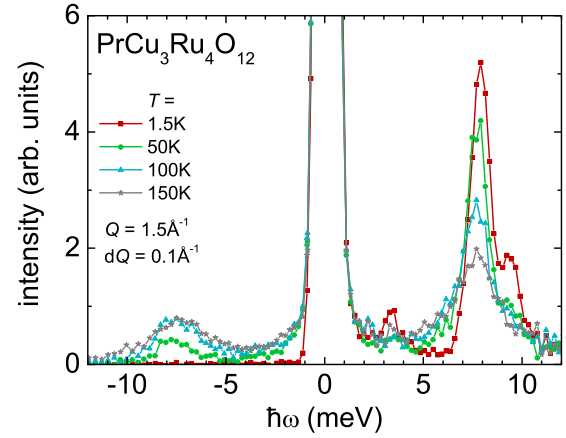

FIG. 14. Dynamic structure factor $S(Q_0, \omega)$ of $PrCu_3Ru_4O_{12}$ for fixed scattering angle (momentum transfer) $Q_0 = 3.5$ Å^{-1} and a width of $dQ_0 = 0.2$ Å^{-1} for various temperatures. Positive values of ω mean energy loss of the neutrons and vice versa.

excitation at 8 meV remains, which can also be observed at the energy gain side.

The detailed evolution of these excitations with temperature is shown in Fig. 14. Representative constant Q scans at a momentum transfer $Q = 3.5$ Å^{-1} for selected temperatures between 1.5 and 150 K indicate a splitting of the excitations at 1.5 K due to a change in symmetry. They get weaker with increasing temperature and eventually vanish such that only the excitation centered at 8 meV remains for $T = 150$ K. This excitation roughly corresponds to a temperature scale of 90 K and represents the splitting of the Pr ground state $\Gamma_4^{(1)}$ to the first excited state Γ_{23} in the cubic crystal field. The additional splittings visible at 1.5 K indicate the substructure of the Pr levels due to further distortion arising from quadrupolar ordering effects.

At this point we would like to comment on possible contributions of phonon scattering in the Q scans investigated. Due to the magnetic form factor, the magnetic intensity decreases with increasing wave vectors and phonon scattering should gain increasing importance. Evaluating the form-factor effect, we find that it could be of the order of 30% in the Q range investigated, but is hardly visible due to the fact that Fig. 13 utilizes a logarithmic intensity scale. The fact that the phonon-induced background is not very important is documented by the constant Q scans shown in Fig. 14, which show very little temperature-dependent background due to phonon scattering. We safely can conclude that phonon scattering does not influence any of the conclusions drawn in this paper.

III. THEORY AND DISCUSSION

A. Cubic crystal field

As mentioned in Sec. II A, $RCu_3Ru_4O_{12}$ (R = La, Pr, Nd) crystallizes in a body-centered-cubic lattice with space group $Im\bar{3}$ (T_h^5) of which the site of the R ion (and thus the CEF symmetry for this site) is represented by the cubic point group $m\bar{3}$ (T_h). According to calculations by Lea *et al.* [37], the Hund's rule ground state of Pr^{3+} ($^3H_4$) in a cubic CEF is split into a nonmagnetic singlet Γ_1, a nonmagnetic doublet Γ_{23}, and two magnetic triplets $\Gamma_{4,5}$. In the case of Nd^{3+} ($^4I_{9/2}$) this

CEF causes a splitting into one magnetic doublet Γ_6 and two magnetic quartets $\Gamma_8^{(1,2)}$.

For a long time it was believed that the same Hamiltonian is applicable to all five cubic point groups [37,80]. However, a reinvestigation of the CEF for the point groups T and T_h shows that this belief is incorrect due to a new nonvanishing term [81]. Although the degeneracy of each sublevel does not change as compared to those of the point group O_h, some eigenfunctions and eigenvalues are affected and therefore the J-manifold diagrams shown in [37] are not relevant in our case (T_h). Note that the symbols of the irreducible representations used below are those according to Ref. [81].

Starting from the CEF Hamiltonian,

$$\mathcal{H}_{\rm cr} = \sum_{k,q} B_q^{(k)} C_q^{(k)}, \tag{2}$$

where

$$C_q^{(k)} = \sqrt{\frac{4\pi}{2k+1}} \sum_i Y_q^{(k)}\{\vartheta_i, \varphi_i\} \tag{3}$$

are operators of the CEF acting on $4f$ electrons and $B_q^{(k)}$ are quantities which in a superposition model [82,83] are calculated as

$$B_q^{(k)} = \sum_j a^{(k)}(R_j) C_{-q}^{(k)}\{\Theta_j, \Phi_j\}, \tag{4}$$

with the so-called intrinsic CEF parameters $a^{(k)}(R_j)$. The index j is running over 12 nearest-neighbor oxygen atoms and 8 next-nearest-neighbor ruthenium atoms ($R_{\text{Pr-O}} = 0.262$ nm and $R_{\text{Pr-Ru}} = 0.323$ nm), while contributions from more distant ions are expected to be negligible. The oxygen atoms form a slightly distorted icosahedron around the R ion with a ratio of the cartesian edge coordinates $b/a = 1.766$ and 1.774 for Pr and Nd at $T = 1.6$ K, respectively [the ideal value $b/a = (1+\sqrt{5})/2 \approx 1.618$]. In contrast, the ruthenium atoms form an ideal cubic configuration. Since the crystallographic differences between the Pr and the Nd compound are marginal, one expects the intrinsic CEF parameters to be roughly the same for both R ions (Pr and Nd). The expressions for the CEF parameters are

$$\begin{aligned}
B_0^{(2)} &= B_2^{(2)} = 0,\\
B_0^{(4)} &= 7a^{(4)}(R_{R\text{-O}})\frac{a^4+b^4-3a^2b^2}{(a^2+b^2)^2}\\
&\quad - \tfrac{28}{9}a^{(4)}(R_{R\text{-Ru}}),\\
B_2^{(4)} &= 0,\\
B_4^{(4)} &= \sqrt{\tfrac{5}{14}}B_0^{(4)},\\
B_0^{(6)} &= \tfrac{3}{4}a^{(6)}(R_{R\text{-O}})\frac{2a^6-15a^2b^4-15a^4b^2+2b^6}{(a^2+b^2)^3}\\
&\quad + \tfrac{16}{9}a^{(6)}(R_{R\text{-Ru}}),\\
B_2^{(6)} &= \frac{33\sqrt{105}}{8}a^{(6)}(R_{R\text{-O}})\frac{a^2b^2(a^2-b^2)}{(a^2+b^2)^3},\\
B_4^{(6)} &= -\sqrt{\tfrac{7}{2}}B_0^{(6)},\\
B_6^{(6)} &= -\sqrt{\tfrac{5}{11}}B_2^{(6)}.
\end{aligned} \tag{5}$$

Note that in the case of the ideal icosahedral symmetry [80]

$$\begin{aligned}
b &= \frac{a(1+\sqrt{5})}{2} = 1.618a,\\
a^4 &+ b^4 - 3a^2b^2 = 0,\\
\frac{a^2+b^2}{a^2-b^2} &= -\sqrt{5},\\
B_0^{(6)} &= -a^{(6)}(R_{R\text{-O}})\frac{33^2b^2}{4(a^2+b^2)^4}.
\end{aligned} \tag{6}$$

Therefore, we expect $B_0^{(6)} < 0$. The situation concerning the sign of the parameter $B_0^{(4)}$ needs some consideration. Definitely $a^{(4)}(R_{R\text{-O}}) > 0$ since the effective electric charge of oxygen and the exchange charge, located at the R-O bond, have the same signs [83,84]. A CEF analysis performed on HoRh on the basis of inelastic neutron scattering [85] showed that $a^{(4)}(R_{\text{Ho-Rh}}) > 0$ and therefore the second term in $B_0^{(4)}$ is negative. Taking into account that the factor $(a^4+b^4-3a^2b^2)/(a^2+b^2)^2$ is just about 0.08, we conclude that the sign of $B_0^{(4)}$ can be negative in $R\text{Cu}_3\text{Ru}_4\text{O}_{12}$ (R = Pr, Nd).

For calculating the relevant wave functions of the respective energy levels, it is useful to separate the Hamiltonian [Eq. (2)] into two terms and write $\mathcal{H}_{\rm cr} = \mathcal{H}_1 + \mathcal{H}_2$. Here $\mathcal{H}_1$ has a form as for conventional cubic (tetrahedral and octahedral) symmetry:

$$\begin{aligned}
\mathcal{H}_1 = B_0^{(4)}&\left[C_0^{(4)} + \sqrt{\tfrac{5}{14}}\left(C_4^{(4)} + C_{-4}^{(4)}\right)\right]\\
&+ B_0^{(6)}\left[C_0^{(6)} - \sqrt{\tfrac{7}{2}}\left(C_4^{(6)} + C_{-4}^{(6)}\right)\right].
\end{aligned} \tag{7}$$

Its wave functions are well known. For the point group T_h one has additional terms due to the lack of umklappung and a fourfold symmetry axis compared to O_h [86]. These terms are represented by $\mathcal{H}_2$ and were found to occur in $R\text{T}_4\text{X}_{12}$ and $R\text{Pd}_3\text{S}_4$ [81]:

$$\mathcal{H}_2 = B_2^{(6)}\left[C_2^{(6)} + C_{-2}^{(6)} - \sqrt{\tfrac{5}{11}}\left(C_6^{(6)} + C_{-6}^{(6)}\right)\right]. \tag{8}$$

Note that for perfect icosahedral symmetry $B_2^{(6)} = \frac{\sqrt{21}}{2}B_0^{(6)}$. This relation illustrates the relative importance of the term $\mathcal{H}_2$ in our case.

Since the R-Ru distance is relatively large (about 3.2285 Å) the contribution related to $a^{(6)}(R\text{-Ru})$ is small with respect to those related to $a^{(6)}(R\text{-O})$. From Eq. (5) it follows that we have just two *a priori* unknown parameters, namely, $B_0^{(6)}$ and $B_0^{(4)}$. Its values are determined on the basis of the above-described experimental data and amount to $B_0^{(4)} = -720 \pm 10$ K and $B_0^{(6)} = -620 \pm 40$ K. Details of the corresponding data analysis $\chi(\text{Pr})$ are given in Sec. III B. They might be of general interest for the analysis of CEF effects concerning R ions in related compounds.

1. Pr^{3+}

In the case of Pr, singlet, doublet, and triplet states correspond to irreducible representations Γ_1, Γ_{23}, and $\Gamma_4^{(1,2)}$,

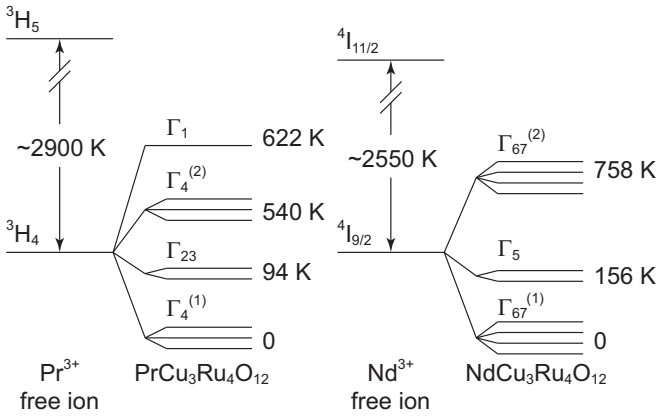

FIG. 15. Level schemes of Pr^{3+} and Nd^{3+} free ions and in $RCu_3Ru_4O_{12}$ (R = Pr, Nd) with corresponding R-site symmetry T_h. Transition energies of the free ions were taken from Ref. [88]. Splittings to the ground state (0) are given in the unit Kelvin.

respectively [81,86,87]. Applying the point group method and diagonalizing $\mathcal{H}_{\rm cr}$, we get the energy levels E,

$$\begin{aligned} E_1 &= -56b_{40} - 80b_{60}, \\ E_{23} &= -8b_{40} + 64b_{60}, \\ E_4^{(1)} &= 12b_{40} - 8b_{60} - 4P_{12}, \\ E_4^{(2)} &= 12b_{40} - 8b_{60} + 4P_{12}, \end{aligned} \tag{9}$$

with $P_{12} = \sqrt{(10b_{40} - 3b_{60})^2 + 60(b_{62})^2}$. Here we have introduced the abbreviations

$$\begin{aligned} b_{40} &= \frac{1}{3 \times 121} B_0^{(4)}, \\ b_{60} &= \frac{4 \times 17}{9 \times 121 \times 13} B_0^{(6)}, \\ b_{62} &= \frac{4 \times 17}{9 \times 121 \times 13} B_2^{(6)}. \end{aligned} \tag{10}$$

Using Eq. (5) and the ratio $b/a = 1.766$, we get $b_{62} = 1.250\frac{\sqrt{21}}{2} b_{60}$. Thus, the crystal-field Hamiltonian $\mathcal{H}_{\rm cr}$ has only two parameters, namely, b_{40} and b_{60}. Based on the experimental data obtained, the dominant CEF excitation at 8 meV between the Γ_4 triplet and the Γ_{23} doublet detected by neutron scattering and the evolution of the magnetic susceptibility performed in Sec. III B and keeping in mind that intrinsic parameters $a^{(k)}$ have to be approximately equal to those of Nd, we get $b_{40} = -2.0$ K and $b_{60} = -3.0$ K. The resulting energy scheme is given in Fig. 15. The ground state is found to be the triplet $\Gamma_4^{(1)}$ and its wave functions are given by

$$\begin{aligned} |1\rangle &= c_1 \frac{1}{\sqrt{8}}[\sqrt{7}|3\rangle - |-1\rangle] - c_2 \frac{1}{\sqrt{8}}[|-3\rangle + \sqrt{7}|1\rangle], \\ |0\rangle &= c_1 \frac{1}{\sqrt{2}}[|2\rangle - |-2\rangle] + c_2 \frac{1}{\sqrt{2}}[|4\rangle - |-4\rangle], \\ |-1\rangle &= -c_1 \frac{1}{\sqrt{8}}[\sqrt{7}|-3\rangle - |1\rangle] + c_2 \frac{1}{\sqrt{8}}[|3\rangle + \sqrt{7}|-1\rangle], \end{aligned} \tag{11}$$

where

$$c_1/c_2 = -2\sqrt{15} b_{62}/(10b_{40} - 3b_{60} + P_{12}). \tag{12}$$

The first excited state is the doublet Γ_{23} and its wave functions are given by

$$\begin{aligned} |\theta\rangle &= \frac{1}{\sqrt{24}}\{-\sqrt{10}|0\rangle + \sqrt{7}[|4\rangle + |-4\rangle]\}, \\ |\varepsilon\rangle &= \frac{1}{\sqrt{2}}[|2\rangle + |-2\rangle], \end{aligned} \tag{13}$$

while the wave functions of the other CEF levels can be written using orthogonality relations.

2. Nd^{3+}

In the case of Nd, doublet and quartet states correspond to irreducible representations Γ_5 and $\Gamma_{67}^{(1,2)}$, respectively [81,87]. By diagonalization of $\mathcal{H}_{\rm cr}$ we get the energy levels E,

$$\begin{aligned} E_5 &= -28d_{40} + 32d_{60}, \\ E_{67}^{(1)} &= 7d_{40} - 8d_{60} - \sqrt{(E_{12})^2 + 240(d_{62})^2}, \\ E_{67}^{(2)} &= 7d_{40} - 8d_{60} + \sqrt{(E_{12})^2 + 240(d_{62})^2}, \end{aligned} \tag{14}$$

with

$$(E_{12})^2 = (10d_{40} - 2d_{60})^2 + \tfrac{3}{7}(25d_{40} + 28d_{60})^2. \tag{15}$$

Here we have introduced the abbreviations

$$\begin{aligned} d_{40} &= \frac{4 \times 7 \times 17}{9 \times 11^3 \times 13} B_0^{(4)}, \\ d_{60} &= \frac{5^2 \times 17 \times 19}{3 \times 11^3 \times 13^2} B_0^{(6)}, \\ d_{62} &= 1.265 \frac{\sqrt{21}}{2} d_{60}. \end{aligned} \tag{16}$$

Since the intrinsic CEF parameters $a^{(4)}(R)$ and $a^{(6)}(R)$ for Nd are approximately the same as for Pr, one expects the following relations:

$$\begin{aligned} d_{40}(\mathrm{Nd}) &\approx 1.1 b_{40}(\mathrm{Pr}), \\ d_{60}(\mathrm{Nd}) &\approx 2.5 b_{60}(\mathrm{Pr}). \end{aligned} \tag{17}$$

The first two wave functions of the ground-state quartet are given by

$$\begin{aligned} \left|\Gamma_{67}^{(1)}, \tfrac{3}{2}\right\rangle &= 0.026\left|-\tfrac{9}{2}\right\rangle + 0.139\left|-\tfrac{5}{2}\right\rangle + 0.199\left|-\tfrac{1}{2}\right\rangle \\ &\quad + 0.468\left|\tfrac{3}{2}\right\rangle - 0.849\left|\tfrac{7}{2}\right\rangle, \\ \left|\Gamma_{67}^{(1)}, \tfrac{1}{2}\right\rangle &= -0.365\left|\tfrac{9}{2}\right\rangle - 0.708\left|\tfrac{5}{2}\right\rangle + 0.246\left|\tfrac{1}{2}\right\rangle \\ &\quad + 0.510\left|-\tfrac{3}{2}\right\rangle + 0.212\left|-\tfrac{7}{2}\right\rangle. \end{aligned} \tag{18}$$

The set of functions for the upper quartet $|\Gamma_{67}^{(2)}, m_s\rangle$ can be written according to orthogonality conditions. The wave functions of the doublet Γ_5 are the same as for the state Γ_6 in generalized cubic symmetry [37,89]. The calculated energy-level diagram is shown for both Pr^{3+} and Nd^{3+} in Fig. 15.

B. Data analysis

To extract the cubic crystal-field parameters we evaluate the magnetic susceptibility data using the expression for the

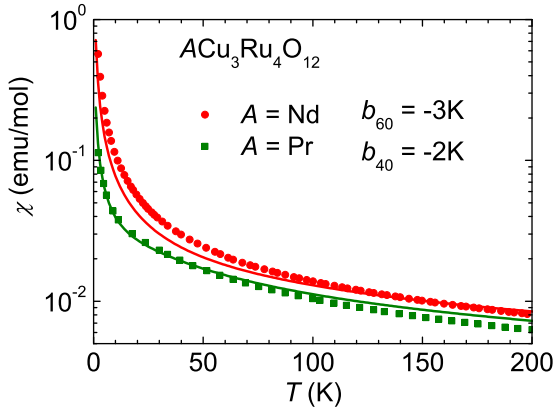

FIG. 16. Temperature-dependent magnetic susceptibility of $RCu_3Ru_4O_{12}$ (R = Pr, Nd) in a semilogarithmic representation and associated fits (solid curves) according to Eq. (A6) with the fitting parameters b_{40} and b_{60} in addition to a Curie-Weiss law.

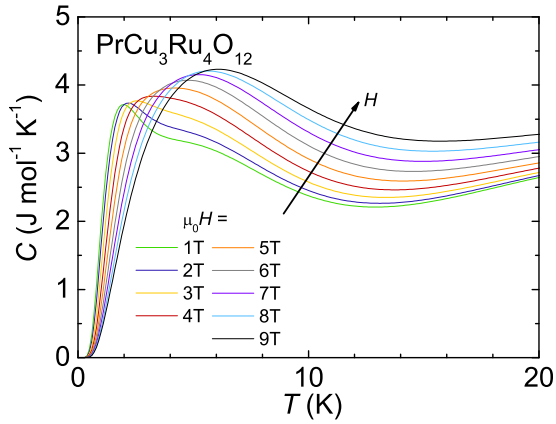

FIG. 17. Calculated temperature-dependent specific heat C (contribution of the CEF only) of $PrCu_3Ru_4O_{12}$ for various magnetic fields based on the local distortions described by Eqs. (19) and (20). See the text for details.

generalized susceptibility [Eq. (A6)] derived in Appendix A, the information from inelastic neutron scattering, and also specific-heat data. For $PrCu_3Ru_4O_{12}$ neutron scattering reveals a splitting of 8 meV between the Γ_4 ground-state triplet and the Γ_{23} excited-state doublet. This is also indicated by the Schottky anomaly centered at 53 K in the specific heat. In $NdCu_3Ru_4O_{12}$ a similar Schottky anomaly appears at 69 K indicating a somewhat larger splitting between the Γ_{67} ground-state quartet and the excited Γ_5 doublet.

Figure 16 shows the fitting of the susceptibility data for $PrCu_3Ru_4O_{12}$ and $NdCu_3Ru_4O_{12}$ with the same parameters B_0^4 and B_0^6 in addition to a Curie-Weiss law for the Cu-Ru spin system with $\theta_{CW}(Nd) = -1000$ K and $\theta_{CW}(Pr) = -1600$ K and a Curie constant $C = 4.54$ emu K/mol according to Ref. [16] for $LaCu_3Ru_4O_{12}$.

Note that subtraction of the susceptibility data of $LaCu_3Ru_4O_{12}$ as reference yields larger effective moments for Pr^{3+} and Nd^{3+} than theoretically expected. Thus, fitting the rare-earth contributions obtained after subtraction by Eq. (A6) results in large deviations at high temperatures. Therefore, we evaluated the original data taking into account the Cu-Ru spin system by an additional Curie-Weiss law with the same Curie constant as for $LaCu_3Ru_4O_{12}$, but using the Curie-Weiss temperature as the fit parameter. By this procedure we obtain a satisfactory description of the susceptibility data of both rare-earth compounds with cubic crystal-field parameters in agreement with the excitation energy between the ground state and the first excited state (see Fig. 15). However, deviations of the fitting for temperatures below 50 K and the appearance of additional excitations in the inelastic neutron scattering measurements at low temperatures make it necessary to take into account local distortions of lower symmetry, which in the $PrCu_3Ru_4O_{12}$ compound results in a singlet ground state.

Clear evidence for local symmetry lowering is provided by the specific-heat data which is shown in Fig. 8. The peak at 2 K indicates splitting of the triplet ground state of the Pr ion. Two reasons for this are possible: first as a result of the lowering symmetry of the crystal lattice and second as an effect of the electric field induced by orbital ordering of quadrupole moments at low temperatures in the sublattice of Pr ions. Such quadrupolar phenomena were found in other Pr compounds too, e.g., evidence for strong quadrupolar pair interactions in rare-earth palladium bronzes RPd_3S_4 [45], multipolar ordering due to antiferro-octupolar interaction at $T_c = 7.5$ K in $Ce(Pd,Pt)_3S_4$ [90], simultaneous antiferro-quadrupolar and ferromagnetic transitions at $T_c = 6.3$ K in $CePd_3S_4$ [91], and antiferroquadrupolar ordering at 3.5 K above the Néel temperature $T_N = 0.7$ K in $DyPd_3S_4$ [92]. These orbital ordering temperatures correspond quite well to the respective one found in $PrCu_3Ru_4O_{12}$ ($T \approx 7$ K; see Fig. 12). In order to get more information about splitting and the ground state, we apply the effective Hamiltonian method [89] and introduce an effective moment $l = 1$ for the triplet ground state of Pr. The effective Hamiltonian with a minimal set of parameters (just two), which allows us to reproduce basic features of temperature and magnetic field dependences of the specific heat, is written as

$$\mathcal{H}_4 = D[3l_z^2 - l(l+1)] + iE'(l_+^2 - l_-^2), \tag{19}$$

with $D = 1.5$ K and $E' = \pm 4.5$ K. The energy levels are given as

$$\begin{aligned} E_1 &= D - 2|E'| = -7.5 \text{ K}, \\ E_2 &= -2D = -3 \text{ K}, \\ E_3 &= D + 2|E'| = 10.5 \text{ K}. \end{aligned} \tag{20}$$

Equation (19) can be interpreted as a result of local distortions of the $4f$-electron density of Pr in the (a, b) plane, which is oriented toward a couple of nearest oxygen positions, forming a dumbbell-like pattern. Our choice of the coordinate system is displayed in Fig. 1. The distortion is uniform along the c axis (one can speculate about ferro-ordered quadrupolar components), but in the (a, b) plane it can be an alternating pattern of p_x and p_y orbitals as well since the sign of the parameter E' is lost during the averaging procedure of the powder sample.

The calculations of the theoretical CEF specific heat for various magnetic fields is shown in Figs. 17 and 18 for Pr and Nd, respectively. Qualitatively, they are in good agreement with the experimental data [see Figs. 8(b) and 9(b)]. Figure 17 shows that a splitting of the Γ_4 ground-state triplet into three

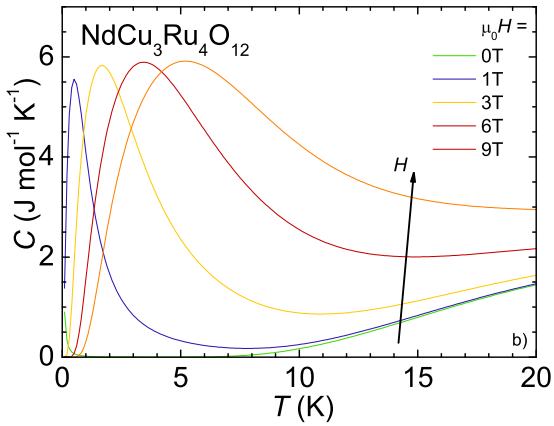

FIG. 18. Calculated temperature-dependent specific heat C (contribution of the CEF only) of $NdCu_3Ru_4O_{12}$ for various magnetic fields based on the local distortions described by Eqs. (19) and (20). See the text for details.

singlets allows us to understand the decreasing amplitude of the Schottky anomaly to low fields in $PrCu_3Ru_4O_{12}$ and the resulting nonmagnetic ground-state singlet. This gives rise to the quadratic field dependence of the Schottky maximum in $PrCu_3Ru_4O_{12}$ (see Fig. 10).

Figure 19 depicts the low-temperature magnetic susceptibility of $PrCu_3Ru_4O_{12}$ in fields up to 14 T. The data have been corrected for the contribution of the reference compound $LaCu_3Ru_4O_{12}$ (1 T data set) and clearly show a significant field-dependent splitting below approximately 10 K. The solid lines have been calculated using the same parameter values as for the specific heat. The susceptibility is suppressed with increasing field and even for small magnetic fields exhibits a saturation toward absolute zero, which is naturally interpreted as evidence of a dominating Van Vleck-type contribution for a singlet ground state. Finally, we have to mention that the

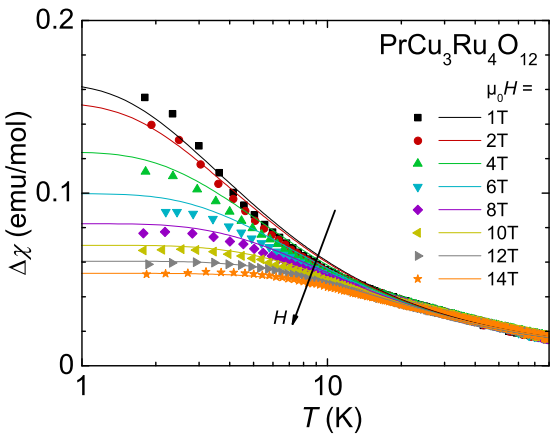

FIG. 19. Temperature-dependent magnetic susceptibility $\Delta\chi$ of $PrCu_3Ru_4O_{12}$ in various magnetic fields in a semilogarithmic representation (symbols). The data have been corrected for the contribution of the reference compound $LaCu_3Ru_4O_{12}$ (1 T data set). The corresponding theoretical modeling is represented by solid curves. The arrow indicates evolution with increasing magnetic field. See the text for details.

overall splitting of the ground-state triplet, which we used to reproduce the low-temperature specific heat and susceptibility, amounts to 18 K, which is only about half of the value found by neutron scattering, 3.5 meV. The reason may be that the real distortion depends on temperature, which is not taken into account by our model and hence an average value of the splitting is anticipated. This may also explain why our model only provides a qualitative description of the low-temperature specific heat and especially why the experimental Schottky anomaly of $PrCu_3Ru_4O_{12}$ does not reveal the substructure visible in our simulation in Fig. 17.

IV. CONCLUSION

We have studied the structural, magnetic, thermodynamic, and transport properties of the A-site ordered perovskite compounds $RCu_3Ru_4O_{12}$ (R = La, Pr, Nd) in a wide range of temperatures ($0.1\ \mathrm{K} \leqslant T \leqslant 750\ \mathrm{K}$) and magnetic fields ($\mu_0 H \leqslant 14$ T). In general, all three compounds exhibit heavy-fermion properties, i.e., an enhanced Sommerfeld coefficient of the specific heat and a quadratic temperature dependence of the electric resistivity, due to strong correlations of the Ru $4d$ electrons. In contrast to $CaCu_3Ru_4O_{12}$, no indications of a valence transition have been detected [15]. This corroborates the stability of the Ru^{4+} valence in the whole temperature regime, in agreement with the observed Curie-Weiss law of the magnetic susceptibility of $LaCu_3Ru_4O_{12}$, which we could now verify up to $T = 750$ K. At the same time this proves the localized nature of the Ru spin.

The magnetic properties of $PrCu_3Ru_4O_{12}$ and $NdCu_3Ru_4O_{12}$ at low temperatures are dominated by the paramagnetism of the R ions. Subtraction of the susceptibility of the La compound from the data of the Pr and Nd compound approximately reveals the proper g values for Pr^{3+} and Nd^{3+}, respectively. Special attention was given to the low-temperature anomalies of magnetization, specific heat, and resistivity in both compounds and their dependence on magnetic field. To analyze them, we studied in detail the peculiarities of CEF effects of the R ions within the point group symmetry T_h. We have demonstrated how the energies and wave functions for Pr and Nd multiplets can be obtained in an analytical way and constructed the complete energy schemes for the ground-state multiplets. The experimental data from neutron scattering, specific heat, and magnetic susceptibility could be successfully interpreted on the basis of this level scheme. The ground states consist of a triplet for Pr^{3+} and a quartet for Nd^{3+}. For both compounds the excited state is a doublet with an excitation energy of 8 meV for Pr and somewhat higher for Nd. At low temperatures local distortions presumably due to orbital ordering result in a further splitting of the ground-state multiplets. In the case of Pr this gives rise to a singlet ground state.

ACKNOWLEDGMENTS

This work was supported by the Deutsche Forschungsgemeinschaft via FOR960 “Quantum Phase Transitions” and the collaborative research center TRR80 “From Electronic Correlations to Functionality.” Part of this work was based on experiments performed at the Swiss spallation neutron source SINQ, Paul Scherrer Institute, Villigen, Switzerland.

Thereby we particularly acknowledge D. Sheptyakov for assisting the SINQ experiments. We also thank D. Vieweg and T. Wiedenmann for experimental support. The authors are grateful to S. G. Ebbinghaus for fruitful discussions and support. The work of M.V.E. was supported in part by the Russian Science Foundation (Project No. 19-12-00244). The work of R.M.E. was done within the framework of fundamental research AAAAA18-118030690040-8 of FRC Kazan Scientific Center of RAS.

APPENDIX A: GENERALIZED SUSCEPTIBILITY AT LOW MAGNETIC FIELDS

We consider the Hamiltonian for a R ion with total spin J_0 exposed to an external field B and to the exchange interaction I_{0l} with l surrounding magnetic ions given by

$$\mathcal{H} = \mathcal{H}_{\rm cr} + \mathcal{H}_{\rm so} + g\mu_{\rm B}\mathbf{JB} + \sum_l I_{0l}(J_0 J_l), \tag{A1}$$

with the crystal field $\mathcal{H}_{\rm cr}$, spin-orbit interaction $\mathcal{H}_{\rm so}$, Zeeman term, and exchange interaction, respectively. Here $\mu_{\rm B}$ denotes the Bohr magneton and g the Landé factor. Then the energy of state $|i\rangle$ up to quadratic terms in the magnetic field B can be written as

$$E_i = \epsilon_i - a_i B_z - c_i B_z^2. \tag{A2}$$

Here, for brevity, we introduce the molecular field parameter $I = \sum_l I_{nl}\langle J_{zl}\rangle$ and

$$\begin{aligned} a_i &= g\mu_{\rm B}\left[1 - \frac{I\chi_{zz}}{(g\mu_{\rm B})^2}\right]\langle i|J_z|i\rangle, \\ c_i &= (g\mu_{\rm B})^2 \\ &\quad \times \sum_j \frac{\langle i|J_z|j\rangle\langle j|J_z|i\rangle}{\epsilon_j - \epsilon_i}\left[1 - \frac{I\chi_{zz}}{(g\mu_{\rm B})^2}\right]. \end{aligned} \tag{A3}$$

Then the susceptibility is calculated via the free energy $F = -\Theta\sum_i \exp(-E_i/\Theta)$ as

$$\begin{aligned} \chi_{zz} = -\frac{\partial^2 F}{\partial B_z^2} &= \frac{1}{\Theta}\sum_i a_i^2\rho_i + 2\sum_i c_i\rho_i \\ &\quad - \frac{B}{\Theta}\sum_i a_i\rho_i \sum_i a_i\rho_i, \end{aligned} \tag{A4}$$

where

$$\begin{aligned} \rho_i &= \frac{1}{Z_0(T)}\exp\left(\frac{-\epsilon_i}{\Theta}\right), \\ Z_0 &= \sum_i \exp\left(\frac{-\epsilon_i}{\Theta}\right). \end{aligned} \tag{A5}$$

The first term in Eq. (A4) corresponds to a Curie-like contribution, the second is the generalized Van Vleck term, and the third one vanishes in our case. Taking into account that the coefficients a_i are dependent on χ_{zz}, we arrive at a generalized Curie-Weiss-Van Vleck expression

$$\chi(T) = \frac{(g\mu_{\rm B})^2\left(\sum_i \rho_i\langle i|J_z|i\rangle^2 + 2\theta\sum_{i,j}\rho_i\frac{\langle i|J_z|j\rangle\langle j|J_z|i\rangle}{\epsilon_j-\epsilon_i}\right)}{\theta + 2I\sum_i \rho_i\langle i|J_z|i\rangle^2 + 2I\theta\sum_{i,j}\rho_i\frac{\langle i|J_z|j\rangle\langle j|J_z|i\rangle}{\epsilon_j-\epsilon_i}}. \tag{A6}$$

Equation (A6) without the molecular field parameter I has been derived previously [93]. From refined evaluation of the low-temperature data we found $I = 0.1$ K for Pr and $I = 0.05$ K for Nd. This is of the order of the magnetic dipole interaction between the rare-earth spins.

APPENDIX B: MAGNETIZATION AND SPECIFIC HEAT

The magnetization per Pr ion is calculated via the free energy

$$M_\alpha(T, H_\alpha) = -\frac{\partial F(T, H_\alpha)}{\partial H_\alpha}, \tag{B1}$$

where

$$F(T, H_\alpha) = -k_{\rm B}T\ln\left(\sum_i e^{\frac{-E_i(H_\alpha)}{k_{\rm B}T}}\right) \tag{B2}$$

and $E_i(H_\alpha)$ are the eigenvalues of the total Hamiltonian $\mathcal{H}_1 + \mathcal{H}_2 + \mathcal{H}_3 + \mathcal{H}_4$. Averaging the magnetic susceptibility over all possible orientations ($H_x = H_y = H_z = H$), i.e., the surface of an ellipsoid gives the simple expression

$$\chi(T, H) = \frac{N}{3}\frac{[M_x(T, H) + M_y(T, H) + M_z(T, H)]}{H}, \tag{B3}$$

with Avogadro number N. The theoretical heat capacity is

$$C(T, H) = \frac{1}{3}\sum_\alpha \frac{\partial F(T, H_\alpha)}{\partial T}. \tag{B4}$$

[1] A. M. Glazer, Acta Crystallogr. B **28**, 3384 (1972).
[2] G. King and P. M. Woodward, J. Mater. Chem. **20**, 5785 (2010).
[3] U. Schwingenschlögl, V. Eyert, and U. Eckern, Chem. Phys. Lett. **370**, 719 (2003).
[4] A. N. Vasil'ev and O. S. Volkova, Low Temp. Phys. **33**, 895 (2007).
[5] M. V. Talanov, Acta Crystallogr. A **75**, 379 (2019).
[6] C. C. Homes, T. Vogt, S. M. Shapiro, S. Wakimoto, and A. P. Ramirez, Science **293**, 673 (2001).
[7] P. Lunkenheimer, R. Fichtl, S. G. Ebbinghaus, and A. Loidl, Phys. Rev. B **70**, 172102 (2004).
[8] Z. Zeng, M. Greenblatt, M. A. Subramanian, and M. Croft, Phys. Rev. Lett. **82**, 3164 (1999).
[9] R. Weht and W. E. Pickett, Phys. Rev. B **65**, 014415 (2001).
[10] W. Kobayashi, I. Terasaki, J. Takeya, I. Tsukada, and Y. Ando, J. Phys. Soc. Jpn. **73**, 2373 (2004).
[11] A. Krimmel, A. Günther, W. Kraetschmer, H. Dekinger, N. Büttgen, A. Loidl, S. G. Ebbinghaus, E.-W. Scheidt, and W. Scherer, Phys. Rev. B **78**, 165126 (2008).
[12] T. T. Tran, K. Takubo, T. Mizokawa, W. Kobayashi, and I. Terasaki, Phys. Rev. B **73**, 193105 (2006).
[13] S. Tanaka, N. Shimazui, H. Takatsu, S. Yonezawa, and Y. Maeno, J. Phys. Soc. Jpn. **78**, 024706 (2009).

[14] H. Kato, T. Tsuruta, M. Matsumura, T. Nishioka, H. Sakai, Y. Tokunaga, S. Kambe, and R. E. Walstedt, J. Phys. Soc. Jpn. **78**, 054707 (2009).

[15] A. Krimmel, A. Günther, W. Kraetschmer, H. Dekinger, N. Büttgen, V. Eyert, A. Loidl, D. V. Sheptyakov, E.-W. Scheidt, and W. Scherer, Phys. Rev. B **80**, 121101(R) (2009).

[16] S. Riegg, S. Widmann, B. Meir, S. Sterz, A. Günther, N. Büttgen, S. G. Ebbinghaus, A. Reller, H.-A. K. von Nidda, and A. Loidl, Phys. Rev. B **93**, 115149 (2016).

[17] M. A. Subramanian and A. W. Sleight, Solid State Sci. **4**, 347 (2002).

[18] S. G. Ebbinghaus, A. Weidenkaff, and R. J. Cava, J. Solid State Chem. **167**, 126 (2002).

[19] M. Labeau, B. Bochu, J. C. Joubert, and J. Chenavas, J. Solid State Chem. **33**, 257 (1980).

[20] J. Muller, A. Haouzi, C. Laviron, M. Labeau, and J. C. Joubert, Mater. Res. Bull. **21**, 1131 (1986).

[21] A. P. Ramirez, G. Lawes, D. Li, and M. A. Subramanian, Solid State Commun. **131**, 251 (2004).

[22] T. Sudayama, Y. Wakisaka, K. Takubo, T. Mizokawa, W. Kobayashi, I. Terasaki, S. Tanaka, Y. Maeno, M. Arita, H. Namatame, and M. Taniguchi, Phys. Rev. B **80**, 075113 (2009).

[23] S. Tanaka, H. Takatsu, S. Yonezawa, and Y. Maeno, Phys. Rev. B **80**, 035113 (2009).

[24] S. G. Ebbinghaus, S. Riegg, T. Götzfried, and A. Reller, Eur. Phys. J.: Spec. Top. **180**, 91 (2010).

[25] N. Büttgen, H.-A. Krug von Nidda, W. Kraetschmer, A. Günther, S. Widmann, S. Riegg, A. Krimmel, and A. Loidl, J. Low Temp. Phys. **161**, 148 (2010).

[26] M. Mizumaki, T. Mizokawa, A. Agui, S. Tanaka, H. Takatsu, S. Yonezawa, and Y. Maeno, J. Phys. Soc. Jpn. **82**, 024709 (2013).

[27] N. Hollmann, Z. Hu, A. Maignan, A. Günther, L. Y. Jang, A. Tanaka, H. J. Lin, C. T. Chen, P. Thalmeier, and L. H. Tjeng, Phys. Rev. B **87**, 155122 (2013).

[28] B. Schmidt, H.-A. K. von Nidda, S. Riegg, S. Ebbinghaus, A. Reller, and A. Loidl, Magn. Reson. Solids **16**, 14210 (2014).

[29] G. M. Kalvius, O. Hartmann, A. Günther, A. Krimmel, A. Loidl, R. Wäppling, K. Sedlak, and R. Scheuermann, J. Phys.: Conf. Ser. **551**, 012015 (2014).

[30] F. Bridges, B. Car, L. Sutton, M. Hoffman-Stapleton, T. Keiber, R. E. Baumbach, M. B. Maple, Z. Henkie, and R. Wawryk, Phys. Rev. B **91**, 014109 (2015).

[31] T. Keiber and F. Bridges, Phys. Rev. B **92**, 134111 (2015).

[32] S. Hébert, R. Daou, and A. Maignan, Phys. Rev. B **91**, 045106 (2015).

[33] S. Riegg, A. Reller, A. Loidl, and S. G. Ebbinghaus, Dalton Trans. **44**, 10852 (2015).

[34] S. Riegg, S. Widmann, A. Günther, B. Meir, S. Wehrmeister, S. Sterz, W. Kraetschmer, S. G. Ebbinghaus, A. Reller, N. Büttgen, H.-A. Krug von Nidda, and A. Loidl, Eur. Phys. J.: Spec. Top. **224**, 1061 (2015).

[35] F. Bridges, Mod. Phys. Lett. B **30**, 1630001 (2016).

[36] T. H. Kao, H. Sakurai, H. Kato, N. Tsujii, and H. D. Yang, J. Phys. Soc. Jpn. **85**, 025001 (2016).

[37] K. R. Lea, M. J. M. Leask, and W. P. Wolf, J. Phys. Chem. Solids **23**, 1381 (1962).

[38] R. Higashinaka, A. Nakama, R. Miyazaki, J. Yamaura, H. Sato, and Y. Aoki, J. Phys. Soc. Jpn. **86**, 103703 (2017).

[39] T. Onimaru and H. Kusunose, J. Phys. Soc. Jpn. **85**, 082002 (2016).

[40] T. Onimaru, K. T. Matsumoto, N. Nagasawa, Y. F. Inoue, K. Umeo, R. Tamura, K. Nishimoto, S. Kittaka, T. Sakakibara, and T. Takabatake, J. Phys.: Condens. Matter **24**, 294207 (2012).

[41] E. D. Bauer, N. A. Frederick, P. C. Ho, V. S. Zapf, and M. B. Maple, Phys. Rev. B **65**, 100506(R) (2002).

[42] Y. Aoki, T. Namiki, S. Ohsaki, S. R. Saha, H. Sugawara, and H. Sato, J. Phys. Soc. Jpn. **71**, 2098 (2002).

[43] K. Tanaka, T. Namiki, A. Imamura, M. Ueda, T. Saito, S. Tatsuoka, R. Miyazaki, K. Kuwahara, Y. Aoki, and H. Sato, J. Phys. Soc. Jpn. **78**, 063701 (2009).

[44] B. Bradlyn, J. Cano, Z. Wang, M. G. Vergniory, C. Felser, R. J. Cava, and B. A. Bernevig, Science **353**, 558 (2016).

[45] K. Abe, J. Kitagawa, N. Takeda, and M. Ishikawa, Phys. Rev. Lett. **83**, 5366 (1999).

[46] P. Fischer, G. Frey, M. Koch, M. Könnecke, V. Pomjakushin, J. Schefer, R. Thut, N. Schlumpf, R. Bürge, U. Greuter, S. Bondt, and E. Berruyer, Physica B **276**, 146 (2000).

[47] H. M. Rietveld, J. Appl. Crystallogr. **2**, 65 (1969).

[48] J. Rodriguez-Carvajal, Physica B **192**, 55 (1993).

[49] R. Bachmann, R. E. Schwall, H. U. Thomas, R. B. Zubeck, C. N. King, H. C. Kirsch, F. J. Disalvo, T. H. Geballe, K. N. Lee, R. E. Howard, and R. L. Greene, Rev. Sci. Instrum. **43**, 205 (1972).

[50] D. Richard, M. Ferrand, and G. J. Kearley, J. Neutron Res. **4**, 33 (1996).

[51] R. W. Grosse-Kunstleve and P. D. Adams, J. Appl. Crystallogr. **35**, 477 (2002).

[52] W. J. A. Peterse and J. H. Palm, Acta Crystallogr. **20**, 147 (1966).

[53] *International Tables for Crystallography*, 4th ed., edited by T. Hahn (Kluwer, Dordrecht, 1996), Vol. A.

[54] H. Kröncke, S. Figge, B. M. Epelbaum, and D. Hommel, *Proceedings of the 37th International School on the Physics of Semiconducting Compounds, Jaszowiec, 2008* [Acta Phys. Pol. A **114**, 1193 (2008)].

[55] M. B. Maple, R. P. Dickey, J. Herrmann, M. C. de Andrade, E. J. Freeman, D. A. Gajewski, and R. Chau, J. Phys.: Condens. Matter **8**, 9773 (1996).

[56] W. G. Penney and R. Schlapp, Phys. Rev. **41**, 194 (1932).

[57] K. Kadowaki and S. B. Woods, Solid State Commun. **58**, 507 (1986).

[58] N. H. Andersen, P. E. Gregers-Hansen, E. Holm, H. Smith, and O. Vogt, Phys. Rev. Lett. **32**, 1321 (1974).

[59] A. I. Abou Aly, S. Bakanowski, N. F. Berk, J. E. Crow, and T. Mihalisin, Phys. Rev. Lett. **35**, 1387 (1975).

[60] P. Fulde, J. Appl. Phys. **49**, 1311 (1978).

[61] M. Yogi, H. Niki, M. Hedo, S. Komesu, and T. Nakama, Physica B **536**, 342 (2018).

[62] C. de la Calle, J. Sanchez-Benitez, F. Barbanson, N. Nemes, M. T. Fernandez-Diaz, and J. A. Alonso, J. Appl. Phys. **109**, 123914 (2011).

[63] T.-H. Kao, H. Sakurai, S. Yu, H. Kato, N. Tsujii, and H.-D. Yang, Phys. Rev. B **96**, 024402 (2017).

[64] H. Kato, T. Tsuruta, T. Nishioka, M. Matsumura, H. Sakai, and S. Kambe, in *Proceedings of the 17th International Conference on Magnetism*, edited by H. Harima, H. Kawamura, Y. Kitaoka, H. Kohno, K. Miyake, Y. Suzuki, H. Sakakima, and G.-q. Zheng [J. Magn. Magn. Mater. **310**, e51 (2007)].

[65] H. Kato, T. Tsuruta, T. Nishioka, M. Matsumura, H. Sakai, and S. Kambe, J. Phys. Chem. Solids **68**, 2187 (2007).

[66] T. Kida, R. Kammuri, M. Hagiwara, S. Yoshii, W. Kobayashi, M. Iwakawa, and I. Terasaki, Phys. Rev. B **85**, 195122 (2012).
[67] T. Kida, R. Kammuri, S. Yoshii, M. Hagiwara, M. Iwakawa, W. Kobayashi, I. Terasaki, and K. Kindo, J. Low Temp. Phys. **159**, 143 (2010).
[68] W. Rong-Juan, Z. Yuan-Yuan, W. Li, L. Yong, S. Jing, X. Rui, and W. Jun-Feng, Chin. Phys. B **24**, 097501 (2015).
[69] I. Terasaki and W. Kobayashi, Prog. Solid State Chem. **35**, 439 (2007).
[70] I. Tsukada, R. Kammuri, T. Kida, S. Yoshii, T. Takeuchi, M. Hagiwara, M. Iwakawa, W. Kobayashi, and I. Terasaki, Phys. Rev. B **79**, 054430 (2009).
[71] A. Tsuruta, T. Itoh, M. Mikami, Y. Kinemuchi, I. Terasaki, N. Murayama, and W. Shin, Materials **11**, 981 (2018).
[72] A. Tsuruta, K. Nomura, M. Mikami, Y. Kinemuchi, I. Terasaki, N. Murayama, and W. Shin, Materials **11**, 1650 (2018).
[73] R. Wang, Y. Zhu, L. Wang, Y. Liu, J. Shi, and R. Xiong, Solid State Commun. **222**, 49 (2015).
[74] H. P. Xiang, X. J. Liu, E. Zhao, J. Meng, and Z. J. Wu, Phys. Rev. B **76**, 155103 (2007).
[75] R. K. Harris, E. D. Becker, S. M. C. De Menezes, R. Goodfellow, and P. Granger, Pure Appl. Chem. **73**, 1795 (2001).
[76] H. Lütgemeier, Hyperfine Interact. **61**, 1051 (1990).
[77] H. E. Stanley, *Introduction to Phase Transitions and Critical Phenomena* (Oxford University Press, New York, 1971), p. 47.
[78] W. Trinkl, N. Büttgen, H. Kaps, A. Loidl, M. Klemm, and S. Horn, Phys. Rev. B **62**, 1793 (2000).
[79] S. A. Al'tshuler and B. M. Kosyrew, *Electron Paramagnetic Resonance*, 1st ed. (Academic, New York, 1964).
[80] U. Walter, J. Phys. Chem. Solids **45**, 401 (1984).
[81] K. Takegahara, H. Harima, and A. Yanase, J. Phys. Soc. Jpn. **70**, 1190 (2001).
[82] D. J. Newman, Adv. Phys. **20**, 197 (1971).
[83] M. V. Eremin and A. A. Kornienko, Phys. Status Solidi B **79**, 775 (1977).
[84] B. Z. Malkin, in *Modern Problems in Condensed Matter Sciences*, edited by A. A. Kaplyanskii and R. M. Macfarlane (Elsevier, Amsterdam, 1987), Vol. 21, Chap. 2, pp. 13–50.
[85] R. Chamard-Bois, J. Rossat-Mignod, K. Knorr, and W. Drexel, Solid State Commun. **13**, 1549 (1973).
[86] A. M. Leushin, Magn. Reson. Solids **21**, 19108 (2019).
[87] H. Bethe, Ann. Phys. (Leipzig) **395**, 133 (1929).
[88] P. L. Scott and C. D. Jeffries, Phys. Rev. **127**, 32 (1962).
[89] A. Abragam and B. Bleaney, *Electron Paramagnetic Resonance of Transition Ions* (Oxford University Press, Oxford, 1970).
[90] S. Michimura, U. Nishikawa, A. Shimizu, M. Kosaka, R. Numakura, R. Iizuka, and S. Katano, Physica B **536**, 1 (2018).
[91] E. Matsuoka, D. Usui, Y. Sasaki, H. Nakao, H. Shida, K. Ohoyama, and H. Onodera, J. Phys. Soc. Jpn. **77**, 114706 (2008).
[92] E. Matsuoka, T. Tayama, T. Sakakibara, Z. Hiroi, N. Shirakawa, N. Takeda, and M. Ishikawa, J. Phys. Soc. Jpn. **76**, 084717 (2007).
[93] L. K. Aminov, B. Z. Malkin, and M. A. Teplov, in *Handbook on the Physics and Chemistry of Rare Earths* (Elsevier, Amsterdam, 1996), Vol. 22, Chap. 150, pp. 295–506.